

Contents

I	A search for highly ionising, short tracks at the CMS detector	1
1	Motivation	3
2	General search strategy	6
2.1	Comparison to earlier searches	10
3	Improved dE/dx measurement for short tracks	12
3.1	Ionisation loss of charged particles	12
3.2	Energy calibration of the silicon pixel tracker	15
3.3	Discrimination of highly-ionising particles	20
3.4	Discrimination improvements	21
4	Simulated samples	25
4.1	Standard Model background samples	25
4.2	Signal samples	26
5	Event selection	28
5.1	Datasets and triggers	28
5.2	Selection of signal candidate events	30
5.2.1	Event-based selection	30
5.2.2	Candidate track selection	32
A	A search for highly ionising, short tracks	41
A.1	Lifetime reweighting	41
A.2	Event yields for simulated samples and data	42
A.3	Signal contamination in validation regions	45
A.4	Validation tests of the background estimation methods	47
A.5	Selection requirements of the “tag-and-probe” samples	49
A.6	Optimisation results with the number of missing outer hits	52
A.7	Underlying distributions for the qualitative search sensitivity optimisation	53
A.8	Trigger emulation	54
A.9	Exclusion limits for all simulated lifetimes	55

29

Part I

30

A search for highly ionising, short tracks at the CMS detector

31

1 Motivation

Supersymmetry is able to offer solutions to many unexplained phenomena in astrophysics and can solve many of the shortcomings of the Standard Model of particle physics (see Section ??). While SUSY has been studied at previous particle colliders including Tevatron and LEP [1,2], the LHC with its high centre-of-mass energy offers a unique opportunity to investigate SUSY models with high sparticle masses that were not accessible in previous experiments.

Therefore, a variety of searches were hunting for SUSY during the run I of the LHC in 2011 and 2012. Proton-proton collision data from the CMS and ATLAS experiments were analysed with a strong focus on the search for SUSY in the strong production sector (e.g. [3–5]). As a consequence, wide, previously unexplored regions of SUSY parameter space are already excluded. However, due to the unknown mechanism of supersymmetry breaking, the most general parametrisation of the Minimal Supersymmetric Standard Model (MSSM) introduces over 100 new parameters and thus opens up an incredibly large phenomenological space. Therefore, SUSY models can lead to a plethora of possible signatures at particle colliders.

(I think it is wrong - What motivation??)

Among more “exotic” SUSY scenarios are models with compressed spectra, where two or more particles are nearly mass-degenerate. Especially scenarios with a wino-like Especially scenarios with a nearly mass-degenerate lightest chargino ($\tilde{\chi}_1^\pm$) and lightest neutralino ($\tilde{\chi}_1^0$) are very interesting from a theoretical and cosmological perspective as they can help to explain the sources of the relic density [6–8]. While it is not possible to explain the full relic density with thermally produced neutralinos for $m_{\tilde{\chi}_1^0} \lesssim 2.9 \text{ TeV}$ [9], neutralinos can still be the dominant part if they are non-thermally produced via the decay of a long-lived particle such as a wino-like chargino. The enhanced annihilation cross section (called Sommerfeld enhancement) into WW -, ZZ - or ff -pairs for a wino-like dark matter candidate leads to an underprediction of the relic density if the neutralino and chargino masses are too small [10]. This underprediction can be cured, however, if there is an additional non-thermal production of dark matter that is caused by the decay of a long-lived chargino. In Supersymmetry, such a mass-degeneracy naturally occurs in case of wino-like neutralinos and charginos, since the mass gap between W_3 and $W_{1/2}$ is fully determined by higher loop corrections (see Section ??).

SUSY scenarios with nearly mass-degenerate particles have two distinctive phenomenological properties that require a very different search strategy compared to general SUSY

searches. First, if the chargino and the neutralino are almost mass-degenerate ($\Delta m \lesssim 200$ MeV), the remaining decay product (e.g. a pion) is very soft in p_T , making it hard to detect. Second, the chargino is long-lived due to phase space suppression (see Section ??) and may traverse several detector layers before decaying. dedx? FIXME

Although supersymmetric models with nearly mass-degenerate $\tilde{\chi}_1^\pm$ and $\tilde{\chi}_1^0$ lead to exotic signatures with long-lived charginos and soft decay products, existing SUSY searches at CMS can in principle be sensitive to these models. The exclusion power of existing SUSY searches can be assessed by interpreting their results in terms of the fraction of excluded parameter points in the phenomenological MSSM (see Section ?? for an introduction to the pMSSM). The results of such a study which has been performed in [11] are shown in Figure 1.1. It can be seen that general SUSY searches (blue area) are sensitive to shorter chargino lifetimes ($c\tau \lesssim 10$ cm). Due to technical reasons¹, the general SUSY searches were never interpreted in the context of SUSY models with longer chargino lifetimes. Two existing searches, the search for long-lived charged particles [12] and the search for disappearing tracks [11] focus on long and intermediate chargino lifetimes, respectively. These two searches (purple and red areas) are sensitive to chargino lifetimes of $c\tau \gtrsim 35$ cm. Taken together, the existing searches exclude a large fraction of pMSSM points at different chargino lifetimes. However, there is a gap between the general SUSY searches and the search for disappearing tracks that is not accessible by any of the existing searches.

The here presented analysis aims at targeting this gap by optimising the search strategy for charginos with intermediate lifetimes of $10 \text{ cm} \lesssim c\tau \lesssim 40 \text{ cm}$. The targeted optimisation strategy is a combination of the strategies used in the search for long-lived charged particles [12] and the search for disappearing tracks [11]. While in [12], the high ionisation losses of hypothetical new massive particles is exploited, it does not take into account whether its reconstructed track is disappearing. In [11], the disappearance of the track is utilised but it does not incorporate the large ionisation losses into the search. Additionally, neither of the search does take into account the possible very short tracks of a early decaying chargino. Thus, the here presented search is the first analysis at CMS combining the two signature properties that are highly distinctive for charginos with intermediate lifetimes: first, the characteristically high ionisation losses of heavy charginos; second, short reconstructed tracks due to chargino decays early in the detector.

The associated challenges and the general search strategy of this analysis will be presented in the next section.

¹The pMSSM interpretation relied on the use of fast simulation techniques which are not capable of simulating charginos with lifetimes $c\tau > 1$ cm.

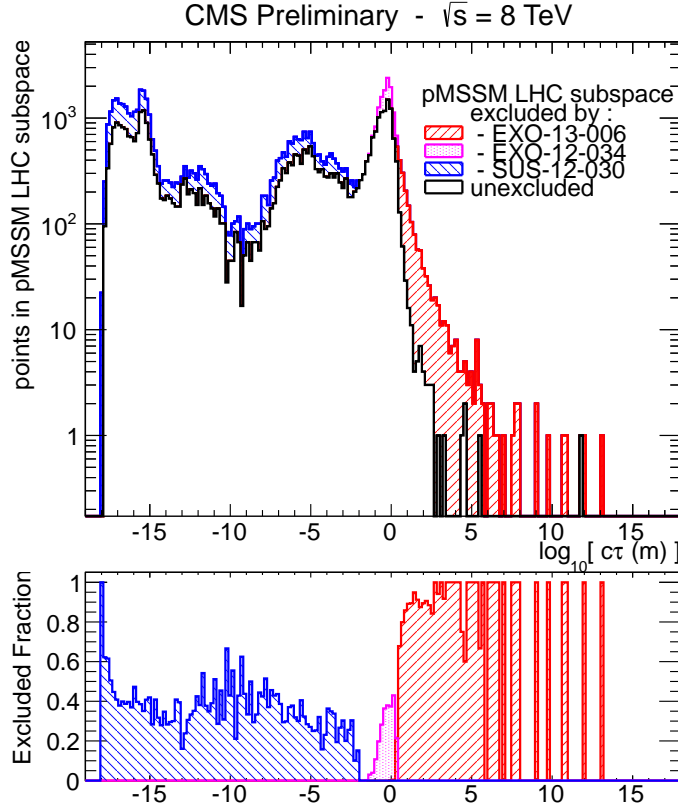


Figure 1.1: The number of excluded pMSSM points at 95% C.L. (upper part) and the fraction of excluded pMSSM points (bottom part) vs. the chargino lifetime for different CMS searches. Red area: the search for long-lived charged particles [12], Purple area: the search for disappearing tracks [11], Blue area: a collection of various general SUSY searches [13] The black line indicates the unexcluded pMSSM parameter points. The sampling of the parameter space points was done according to a prior probability density function which takes pre-LHC data and results from indirect SUSY searches into account (see [14] for further details). Taken from: [15].

2 General search strategy

At the LHC, there are several possible chargino production channels. Chargino pairs can be produced through a photon or a Z -boson exchange. The chargino then decays via a virtual W -boson to the lightest neutralino and a fermion pair (e.g. a pion). This process is illustrated in the Feynman diagram in Fig. 2.1. Other possible chargino pair production channels include the exchange of a supersymmetric Higgs boson or a t -channel squark exchange (Fig. 2.2).

Apart from pair production, charginos can be produced via the chargino neutralino production channel. On tree-level, there exist two production mechanisms: the s -channel W -boson exchange and the t -channel squark exchange (Fig. 2.3).

Alternatively, charginos can be produced via strong production modes, i.e. in cascade decays of new heavy particles, such as gluinos or squarks. In the here presented search, the focus is, however, put on the electroweak production channels: chargino-pair and chargino-neutralino production.

When searching for supersymmetric models with long-lived $\tilde{\chi}_1^\pm$, the strategy is of course highly dependent on the actual lifetime of the chargino. For long lifetimes, the chargino

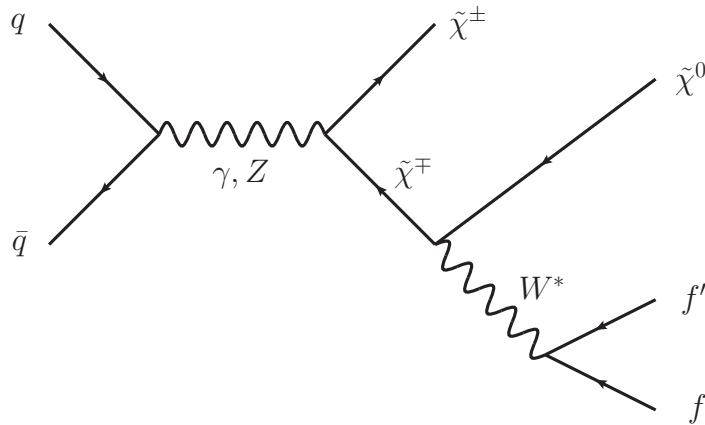


Figure 2.1: Feynman diagram of chargino pair production via gamma or Z -boson exchange and the subsequent decay via a virtual W -boson.

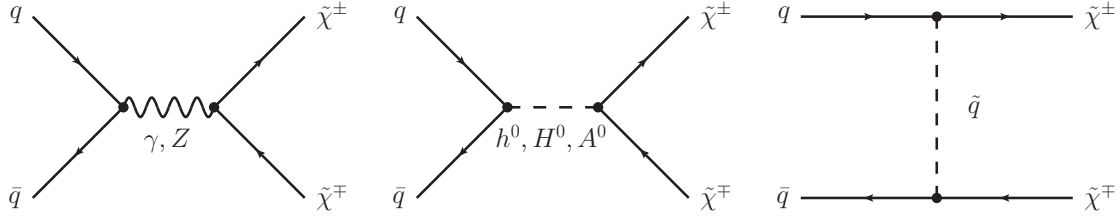


Figure 2.2: Main tree-level diagrams for chargino pair production.

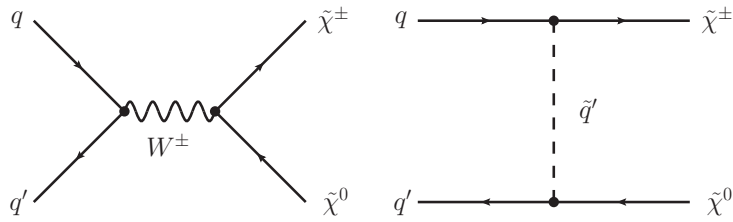


Figure 2.3: Main tree-level diagrams for chargino neutralino production.

can reach the muon chambers and can be reconstructed as a muon even despite a longer time-of-flight [16]. For lower lifetimes, the chargino can already decay inside the detector (e.g. the tracker), and can hence not be reconstructed as a muon but leads to an isolated, potentially disappearing track in the tracker. The detector signatures of these two scenarios are visualised in Fig. 2.4, where simulated chargino-chargino events are shown in a cross-sectional view of the CMS detector. In the left picture of Fig. 2.4, both charginos are reconstructed as muons, which can be seen in the energy deposition in the muon chambers. In the middle and right pictures both charginos have a lower lifetime of $c\tau = 0.5$ m and thus are only visible as tracks in the tracker, where both trajectories end inside the silicon strip tracker. Since this analysis targets a search for Supersymmetry with charginos of lifetimes between $c\tau \approx 10$ cm – 40 cm, the charginos decay rather early in the detector, even in the inner layers of the tracker. Thus, the signature of chargino events consists of isolated, short tracks and the signatures of the decay products, i.e. of a neutralino and a fermion pair.

In case of R-parity conservation one of the chargino decay products, the neutralino, is stable and weakly interacting, thus traversing the detector without leaving any further signature.

The signature of the other decay product, the fermion pair, can in principle be used to select chargino events. However, for mass-degenerate charginos, it can be very hard or even impossible to detect these fermions as will be explained in detail in the next paragraph.

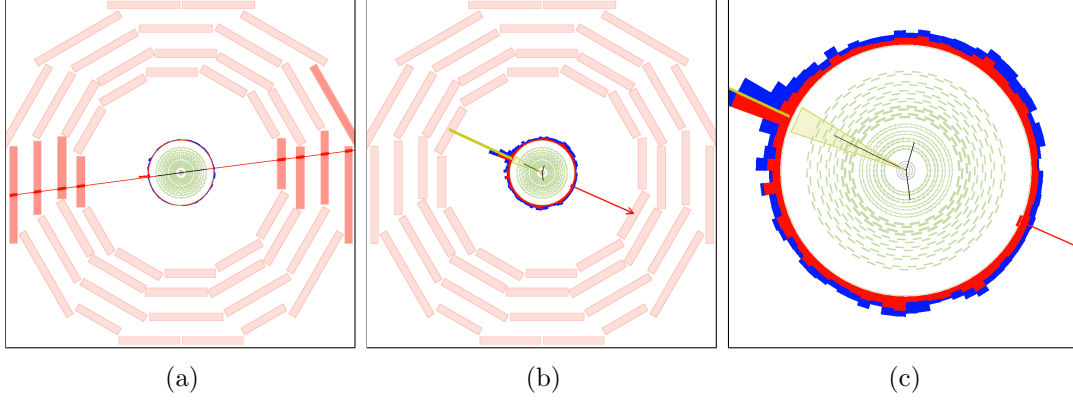


Figure 2.4: Visualisation of possible signatures of a chargino pair produced with a lifetime of $c\tau = 10$ m (a) and a lifetime of $c\tau = 0.5$ m (b and c). The muon chambers are the outer layers of the detector and are depicted as red boxes. The black lines represent the reconstructed chargino tracks. The right picture is a zoom of the picture in the middle. Here, only the cross-section of the tracker (green wavy lines for the strip and grey lines for the pixel) is displayed. The red arrow shows the missing transverse energy in the event. The red (blue) towers correspond to the energy deposition in the ECAL (HCAL).

137 First of all, the fermionic decay product (e.g. a pion) can usually not be reconstructed
 138 because it does not origin from the primary vertex. Secondly, it is very low in momentum
 139 because of the mass-degeneracy between $\tilde{\chi}_1^\pm$ and $\tilde{\chi}_1^0$. The typical momentum of a pion
 140 originating from a chargino to neutralino decay in the $\tilde{\chi}_1^\pm$ rest frame is of the order

$$p_\pi \sim \sqrt{m_{\tilde{\chi}_1^\pm} - m_{\tilde{\chi}_1^0} - m_\pi}. \quad (2.1)$$

141 For a mass gap between $\tilde{\chi}_1^\pm$ and $\tilde{\chi}_1^0$ of $\Delta m = 150$ MeV, the pt distribution of the resulting
 142 pion peaks at ~ 100 MeV and ends at $p_T \sim 400$ MeV (Fig. 2.5).

143 If the transverse momentum of a particle is very low, the particle trajectory is much more
 144 bended compared to a particle with higher p_T (see Fig. 2.6 for illustration). Due to this
 145 bending, the track reconstruction efficiency of particles with a transverse momentum below
 146 1 GeV decreases rapidly, reaching around 40% for isolated pions with a p_T of 100 MeV [17].
 147 Furthermore, for pions that are not produced in the primary vertex, this reconstruction
 148 efficiency will be even smaller. It is therefore impossible to rely on a reconstruction of the
 149 fermionic chargino decay products in this analysis.

150 In summary, since an early decaying chargino is not reconstructed as a PF particle,
 151 the event signature of a chargino-pair or a chargino-neutralino event consists only of one
 152 (or two) - potentially - disappearing track. Such a signature is very difficult to detect,
 153 especially since CMS doesn't offer a dedicated track trigger so that triggering on the

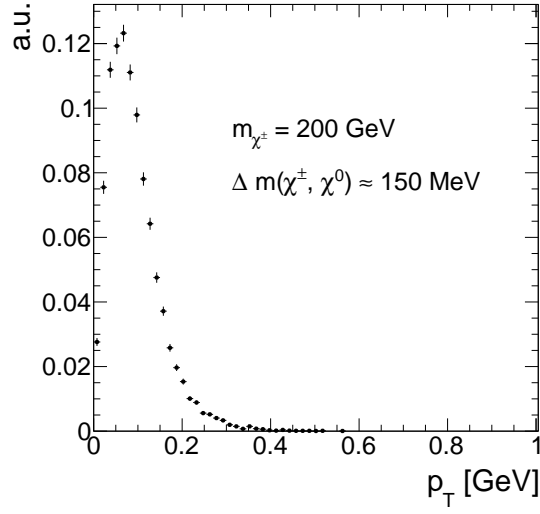


Figure 2.5: Transverse momentum distribution of pions coming from chargino decay into a neutralino with a mass gap of 150 MeV.

154 chargino track is impossible.

155 In order to search for such signatures, one therefore needs to trigger on other, less obvious
 156 properties of chargino events. This analysis takes advantage of higher order contributions
 157 to the Feynman diagrams shown in Figs. 2.2 and 2.3, resulting in initial state radiation
 158 (ISR). If the initial quarks radiate a high p_T gluon, the resulting jet can be detected and can
 159 offer a possibility to search for events with nothing more than isolated tracks. Furthermore,

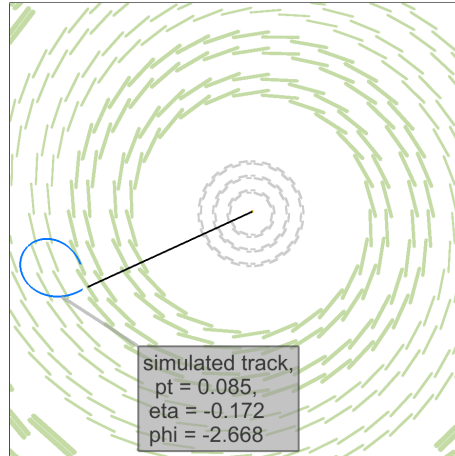


Figure 2.6: Cross-sectional view of the tracker (silicon strip (silicon pixel) tracker layers are illustrated with green (grey) lines) and a simulated chargino track (black line) decaying to a pion (bended blue line) with a p_T of ~ 85 MeV and a neutralino (not visible).

the non-detection of the chargino's decay products plus a high p_T ISR jet lead to missing transverse energy (MET) in the event. Exploiting these two circumstances, it is possible to detect chargino-pair or chargino-neutralino events with the help of Jet+MET triggers.

Since Jet+MET triggers are not very specific for chargino events, it is important to identify further track properties that can be used to select chargino candidates. One distinctive property of charginos compared to SM particles is their high mass. Therefore, charginos can be identified by selecting high p_T tracks. Furthermore, the energy loss per path length (dE/dx) depends quadratically on the particle's mass for low velocities ($0.2 < \beta\gamma < 0.9$):

$$\left\langle \frac{dE}{dx} \right\rangle = K \frac{m^2}{p^2} + C$$

Therefore, dE/dx constitutes a very nice discriminating variable for massive particles like charginos against SM particles. The selection of chargino events in this analysis thus relies on the selection of isolated high p_T tracks with high dE/dx values.

If the chargino decays before it has crossed the full pixel and strip detector, the associated track is disappearing. For low lifetimes, the tracks can be very short and can have only a few hits in the detector. In order to reconstruct a particle's trajectory, a minimum of three hits are required since defining a helical path requires five parameters (see [17]). A specific challenge for this analysis is hence the combination of searching for short tracks and utilising the measurement of the energy deposition of the chargino. For very short tracks, eventually only passing the first couple of layers of the whole tracker system, the pixel tracker information becomes very important. Therefore, an accurate energy measurement in the pixel system is of great importance to this analysis. However, no other CMS analysis has used the energy information of the pixel tracker so far. This analysis thus requires a thorough study of the quality of the pixel energy calibration and, potentially, a recalibration in case the pixel energy calibration is not sufficient.

2.1 Comparison to earlier searches

As already mentioned before, there are two analyses at CMS at $\sqrt{s} = 8$ TeV with 20 fb^{-1} data that search for intermediate lifetime charginos, the search for long-lived charged particles [12] and the search for disappearing tracks [11]. The here presented analysis aims at achieving an increase in sensitivity towards shorter lifetimes compared to the earlier analyses in a twofold way. First, the selection is optimised for the inclusion of very short tracks. Second, the inclusion of the variable dE/dx is used to increase the search sensitivity compared to [11].

In [12], a minimum number of eight hits were required for every track, whereas [11] required a minimum of seven hits. This can be very inefficient for shorter lifetimes, where

most of the charginos already decay shortly after the pixel tracker. In Fig. 2.7 (left), the normalised distribution of the number of measurements (N_{hits}) of chargino tracks is shown. It can be seen, that N_{hits} peaks at the minimal possible value needed for track reconstruction of $N_{\text{hits}} = 3$ for lower lifetimes. For a lifetime of $c\tau = 50$ cm, a second peak at ~ 17 hits appears corresponding to the number of measurements when crossing all pixel barrel (3) and strip inner and outer barrel (6 from stereo and 8 from normal) layers. However, a notable fraction of $\sim 40\%$ of chargino tracks still has a number of measurements of $N_{\text{hits}} < 8$.

It should be also mentioned, that the track reconstruction efficiency is sufficient for short chargino tracks, such that a loosening of the N_{hits} requirement is expected to be really improving the signal acceptance. The track reconstruction efficiency for different chargino decay points is depicted in Fig. 2.7 (right). For very short tracks ($N_{\text{hits}} = 3$) the efficiency is still around 20%.

Additionally, the search for disappearing tracks which targets models with charginos decaying inside the tracker did not make use of the high energy deposition of heavy particles. Although this variable was indeed used in the search for long-lived charged particles, this search was not optimised for intermediate lifetimes (e.g. no explicit muon veto on the selected tracks was required). Thus, it shows less sensitivity compared to the disappearing track search in the lifetime region between $35 \text{ cm} \lesssim c\tau \lesssim 100 \text{ cm}$ (see Fig. 1.1).

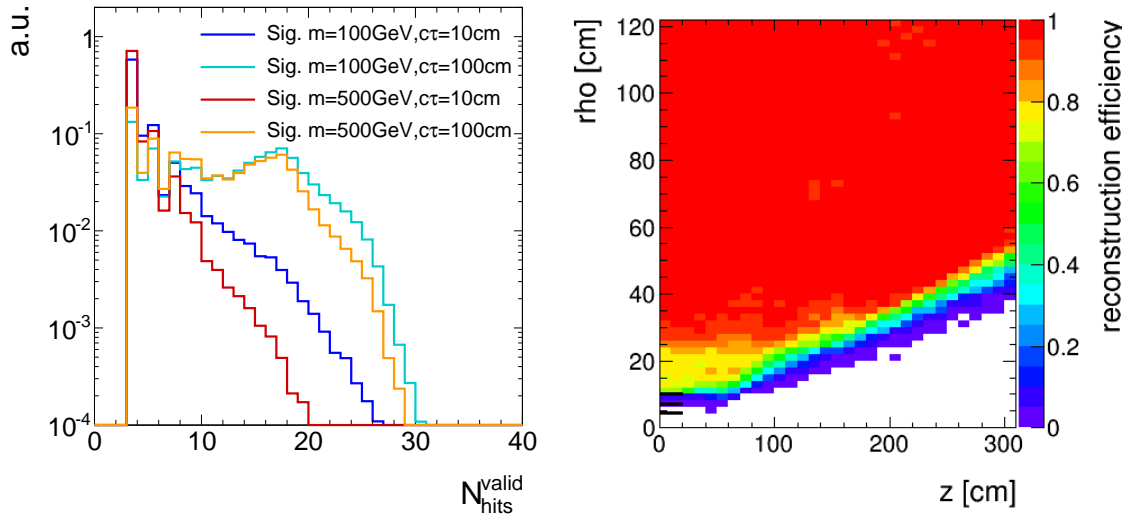


Figure 2.7: Left: Number of measurements in the tracker system N_{hits} for four different signal lifetimes. Right: Probability to reconstruct a track (z) in dependency of the chargino's decay point (x and y). More information on the generation of the simulated signal samples can be found in Section 4.2.

215

216 To conclude, the general search strategy of the here presented analysis is to unite the
 217 strategies of [12] and [11] and to lower the strong selection on the number of hits in these
 218 analyses in order to get an optimised selection for lifetimes around $10\text{ cm} \lesssim c\tau \lesssim 40\text{ cm}$.

219 3 Improved dE/dx measurement for short tracks

220 As already pointed out in the previous chapter the inclusion of the pixel energy measure-
 221 ments can increase the sensitivity when searching for short and highly ionising tracks.
 222 While the silicon strip detector has already been calibrated as part of the search for long-
 223 lived charged particles [12], no complete calibration has been done for the pixel silicon
 224 tracker so far. To increase the discrimination power of dE/dx for short tracks, such a
 225 calibration procedure is therefore conducted within this PHD thesis.

226 The CMS tracker system provides a measurement of the particle's energy loss for each
 227 hit in the tracker. This is done by the detection of the number of electrons produced by
 228 the ionisation of the silicon. A detailed introduction to the CMS tracker system and the
 229 energy measurement can be found in Section ??.

230 How to combine the single energy measurements for each tracker hit into one track
 231 dE/dx estimator that can be used for analysis purposes will be explained in the follow-
 232 ing Section 3.1. The pixel energy calibration is then described in Section 3.2. How to
 233 discriminate SM particles and beyond SM particles with the help of a dE/dx measure-
 234 ment is discussed in Section 3.3, followed by the exploration of the achieved discrimination
 235 improvements in Section 3.4.

236 3.1 Ionisation loss of charged particles

237 Energy losses for moderately relativistic charged particles travelling through matter are
 238 mostly caused by ionisation effects. The mean energy loss per path length can be described
 239 with the Bethe formula [18]:

$$\langle \frac{dE}{dx} \rangle = K z^2 \frac{Z}{A} \frac{1}{\beta^2} \left[\frac{1}{2} \ln \frac{2m_e c^2 \beta^2 \gamma^2 T_{\max}}{I^2} - \beta^2 - \frac{\delta(\beta\gamma)}{2} \right]. \quad (3.1)$$

240 It is a function of the atomic number (Z), the atomic mass (A) of the absorber, and the
 241 mean excitation energy (I) which is 173 eV for silicon [19]. T_{\max} represents the maximum
 242 energy transfer in a single collision. The relevant particle's properties are the velocity (β),
 243 the Lorentz factor (γ) and the charge (z) of the incident particle. The density correction

$\delta(\beta\gamma)$ reduces the mean energy loss at high energies because of polarisation effects of the material. The factor K is constant and is 0.307 in units of $\text{MeV mol}^{-1}\text{cm}^2$. The Bethe formula is valid if the main energy loss originates from ionisation effects, i.e. in a region between $0.1 \lesssim \beta\gamma \lesssim 1000$.

Even if widely used, the mean energy loss is a quantity which is “ill-defined experimentally and is not useful for describing energy loss by single particles” [20]. The problem is caused by the underlying probability distribution of one single dE/dx measurement (this will be named $\Delta E/\Delta x$ throughout the following sections), which can be parametrised by a Landau distribution [21]

$$p(x) = \frac{1}{\pi} \int_0^\infty e^{-t \log t - xt} \sin(\pi t) dt. \quad (3.2)$$

The Landau distribution has no free parameters. Its most probable value is around 0.222. However, it is possible to introduce artificially a different most probable value and a width (at half maximum) with $x \rightarrow \frac{x - \text{MPV}}{\sigma} - 0.222$. The Landau distribution is a highly asymmetric distribution with a long tail towards the right end (see Fig. 3.1). Theoretically it extends to infinite energies, however in nature the maximal deposited energy is of course limited by the particle’s full energy. Because of its strong asymmetry, measurements of the mean energy loss per path length $\langle dE/dx \rangle$ with only a few single measurements are easily fluctuating towards high values. This makes the use of the mean energy loss described by the Bethe formula for the discrimination of new heavy particles problematic, because massive particles release in general higher amounts of energy in matter.

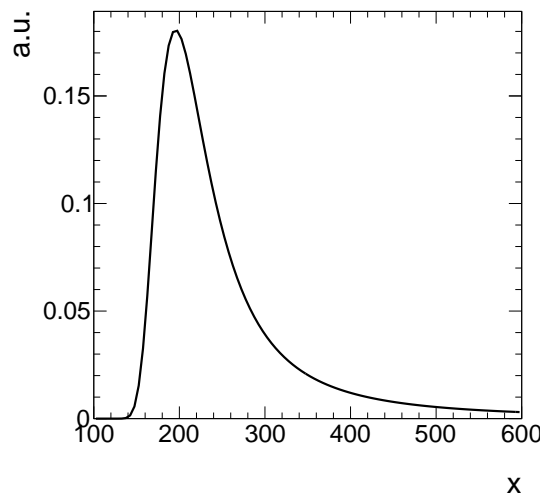


Figure 3.1: Illustration of the shape of a Landau distribution. Parameters were chosen as $\mu = 200$ and $\sigma = 20$.

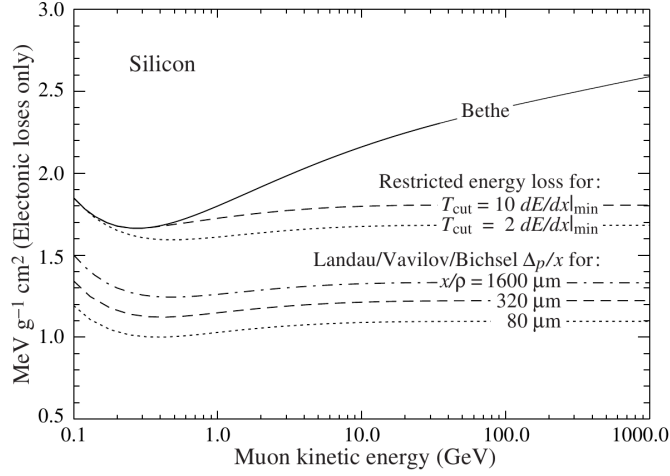


Figure 3.2: Comparison between the Bethe mean energy loss, restricted energy loss and the most probable energy loss described by the Landau-Vavilov-Bichsel function for muons for different values of absorber thickness of silicon. Taken from [20].

263 A much better observable is the most probable value (MPV) of the Landau distribution.
 264 The MPV is much more stable compared to the mean and is not as easily fluctuating to
 265 higher dE/dx values. The most probable energy loss of a charged particle, Δ_p , can be
 266 described by the Landau-Vavilov-Bichsel equation [22]:

$$\Delta_p = \xi \left[\ln \frac{2m_e c^2 \beta^2 \gamma^2}{I} + \ln \frac{\xi}{I} + j - \beta^2 - \delta(\beta\gamma) \right], \quad (3.3)$$

267 with $\xi = (K/Z)\langle Z/A \rangle (x/\beta^2)$. The thickness of the absorber x appears explicitly in
 268 the Landau-Vavilov-Bichsel equation making the most probable energy loss per path
 269 length Δ_p/dx logarithmically dependent on x . A comparison between the Bethe mean
 270 energy loss $\langle dE/dx \rangle$ and the most probable energy loss Δ_p/dx for muons is shown in
 271 Fig. 3.2.

272 Particles such as muons are minimally ionising in silicon for $\beta\gamma \sim 3 - 4$. For higher
 273 momenta the deposited energies increase again reaching a plateau at around $\beta\gamma \sim 100$.
 274 However, new heavy charged particles would mainly be unrelativistic because of their high
 275 mass and would therefore deposit much higher energies in the detector. This makes dE/dx
 276 a very well discriminating variable. Thus, the energy loss per path length can be used to
 277 discriminate between SM particles and new heavy charged particles due to the different
 278 velocity distributions.

279

280 As said before, the most probable energy loss is much more stable compared to the
 281 Bethe mean energy loss. Still, combining only a few measurements of $\Delta E/\Delta x$ can also

lead for Δ_p/dx to large fluctuations towards high dE/dx values. In order to estimate experimentally the most probable dE/dx value from only a few energy measurements, several “estimators” can be used that suppress a potential bias towards the high end without introducing a bias towards lower values [23]. One of the estimators for determining a track’s dE/dx is the harmonic-2 estimator

$$I_{h2} = \left(\frac{1}{N} \sum_{i=1}^N (\Delta E_i / \Delta x_i)^{-2} \right)^{-1/2}, \quad (3.4)$$

where $\Delta E_i / \Delta x_i$ corresponds to the ΔE and Δx measurement in the i th hit of the track. This estimator is known to be robust and not be easily biased by large fluctuations in $\Delta E / \Delta x$ because of the suppression by a factor of two.

The harmonic-2 estimator is also used for the pixel energy calibration described in the following section.

3.2 Energy calibration of the silicon pixel tracker

During Run I in 2012, the pixel silicon detector was continuously subjected to an energy calibration, a so-called gain calibration. Every pixel was calibrated to the same response, so that the whole pixel tracker should have been well inter-calibrated [24]. Unfortunately, due to various reasons, such as the imperfect constancy of the reference signal, or radiation and temperature induced changes, the energy calibration could not ensure a fully calibrated pixel tracker. This imperfection of the gain calibration can be seen in Fig. 3.3, where the mean of the harmonic-2 estimator for all tracks $\langle I_{h2} \rangle$ over the full data-taking period in 2012 is shown. Four different steps can be spotted. The first and the third steps correspond to changes in the settings of the tracker due to irradiation. The second and fourth step are induced by associated adjustments in the online gain calibration. Unfortunately, although the gain calibration was adjusted (even with some delay), it was not able to ensure a constant energy response of the pixel tracker over time. The variations of the dE/dx measurement over time of around 15% are too large to use dE/dx without a further calibration.

The following sections explain the method of the gain calibration of the pixel silicon tracker which is conducted for this analysis. It is splitted into two sections. The first section is dedicated to the gain inter-calibration of the pixel tracker which ensures a homogeneous energy response of all tracker modules. In the second section, the absolute gain calibration is discussed. This calibration step is needed to ensure that the measurement of the energy release of a particle is actually translated to the correct physical value.

Detailed technical information about the pixel tracker can be found in Section ??.

314 Inter-calibration of gain

315 The main goal of the gain calibration is to get a uniform response in the ionisation energy
 316 loss dE/dx over the full data taking period in 2012. To also ensure a uniform response
 317 over all modules within one time step, an additional inter-calibration on module level is
 318 carried out. The inter-calibration can in principle be done on various levels: the highest
 319 granularity would be a calibration on pixel level, followed by a calibration on read-out-
 320 chip (ROC) level and then on module-level. Lower granularities in descending order are
 321 rings (modules with same z-position) and finally layers (3 layers in the barrel and 4 disks
 322 in the endcap). It is checked that all pixels and all ROCs (on one module) are well
 323 inter-calibrated, such that the inter-calibration is finally done module-wise.

324 The gain calibration of the pixel silicon tracker is carried out with the help of minimally
 325 ionising particles (MIPs). MIPs in this context are not defined as particles depositing a
 326 minimum amount of energy, but more generally a small amount of energy. This denotes
 327 all particles located at or near the plateau of the most probable dE/dx distribution vs.
 328 momentum (see Fig. ??). This approach ensures that all particles deposit similar amounts
 329 of energy so that the variation due to different momenta is minimised. MIPs are selected
 330 by a momentum selection of $p > 2$ GeV. Additionally, only tracks with at least eight
 331 hits and a $\chi^2/\text{n.d.o.f.} < 3$ are used to ensure a high-quality track reconstruction. A
 332 sample containing around 50 million “minimum bias” events is used for calibration. The
 333 “minimum bias” sample was specifically recorded for tracker calibration purposes.

334 For every module in the pixel tracker (there are 1440 modules in total), a distribution
 335 of the energy loss per path length $\Delta E/\Delta x$ is built. The measurement of $\Delta E/\Delta x$ is

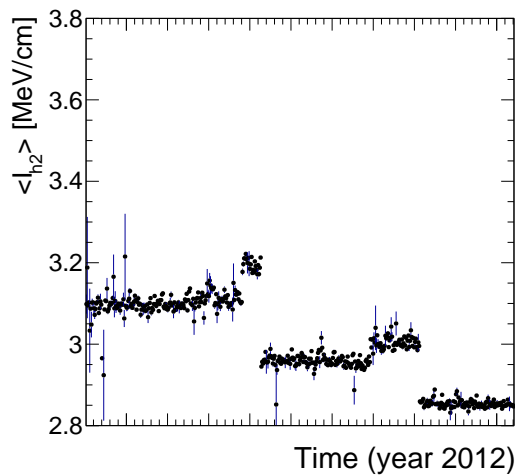


Figure 3.3: Mean of all track's dE/dx (harmonic-2 estimator) over the full year 2012. Only pixel hits are taken into account. Every data point corresponds to one run.

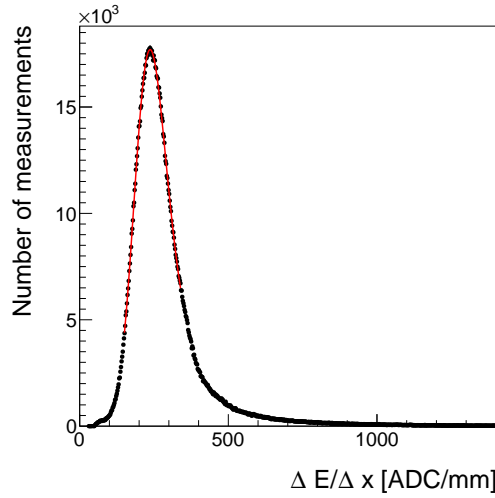


Figure 3.4: An example of the $\Delta E/\Delta x$ distribution measured in ADC count per mm for one module of the CMS pixel tracker. A Landau convoluted with a Gaussian is fitted to the core of the distribution in an iterative procedure.

done in ADC counts per mm. ADC counts are a measure for the deposited charge after digitisation. Figure 3.4 shows an example distribution for one module. The underlying Landau distribution can be nicely seen. To extract the MPV for every module a fit to the core distribution is performed. The fit is not only done with a Landau but a Landau convoluted with a Gaussian function to be closer to the experimentally observed energy spectrum. This also increases the fit performance and the stability of the fit. The path length Δx is calculated with

$$\Delta x = d_{\text{module}_i} \cdot \cos(\phi_{\text{track}}), \quad (3.5)$$

where d_{module_i} is the thickness of module i and ϕ_{track} is the relative angle of the particle's trajectory to the normal axis of the module. With the measured MPV extracted from the fit, an inter-calibration factor is calculated for every module

$$c_{\text{inter}} = \frac{\text{MPV}_{\text{target}} [\text{ADC/mm}]}{\text{MPV} [\text{ADC/mm}]} = \frac{300 \cdot 265 \text{ ADC/mm}}{\text{MPV} [\text{ADC/mm}]}. \quad (3.6)$$

The factor $300 \cdot 265 \text{ ADC/mm}$ is in principal an arbitrary number since the final response is adjusted by the absolute gain calibration described in the next section. However, it is chosen such that the measured calibration factors are close to one. The calibration factor can then be used to scale every single measurement in a module to a calibrated

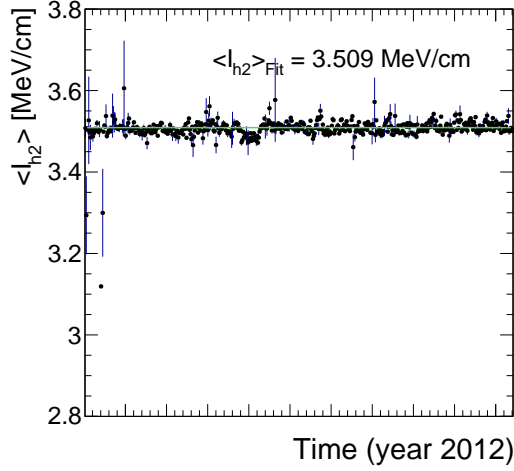


Figure 3.5: Mean of all track's dE/dx (harmonic-2 estimator) over the full year 2012 after applying the calibration factors, resulting in an average dE/dx of 3.51 MeV/cm. Only pixel hits are taken into account. Every data point corresponds to one run.

350 $\Delta E/\Delta x$ measurement

$$\frac{\Delta E}{\Delta x_{\text{calibrated}}} = c_{\text{inter}} \cdot \frac{\Delta E}{\Delta x_{\text{uncalibrated}}} \quad (3.7)$$

351 The determination of the calibration factor is done for every of the five time steps,
 352 shown in Fig. 3.3 independently, in order to get rid of the time dependency. The outcome
 353 of the application of the calibration factors to the single energy measurements in the pixel
 354 tracker can be seen in Fig. 3.5. The variation over time is indeed eliminated, resulting in
 355 a maximal time variation of less than $\sim 1\%$.

356 Additionally, the same procedure is carried out for a corresponding simulated data
 357 sample to ensure the inter-calibration of the pixel modules on all simulated samples.

358 Absolute calibration of gain

359 As a final step, the targeted MPV being $\text{MPV}_{\text{target}} = 300 \cdot 265 \text{ ADC/mm}$ needs to be
 360 translated to a meaningful physical quantity given in physical units (e.g. MeV/cm). That
 361 means, that the charge measurement in ADC counts needs to be converted to the real
 362 energy release of a particle. The relation between ΔE in ADC counts and the energy loss
 363 in eV is given by

$$\Delta E [\text{eV}] = c_{\text{inter}} \cdot \Delta E [\text{ADC}] \cdot \frac{N_e}{\text{ADC}} \cdot 3.61 \text{ eV}, \quad (3.8)$$

where N_e/ADC is the number of electrons which correspond to one calibrated ADC count and 3.61 eV is the mean energy needed to create one electron-hole pair in silicon at -10°C. Such an absolute gain calibration can be done with the help of several methods (all explained in [23]). The absolute calibration of the silicon pixel tracker can rely on the already conducted absolute calibration of the silicon strip detector. In [23], the absolute gain calibration was done with the help of the most probable energy release per path length of muons, theoretically described by the Landau-Vavilov-Bichsel formula in Eq. (3.3). To calibrate the pixel tracker to the correct energy loss per path length it is therefore sufficient to determine one calibration factor to relate the average dE/dx of all tracks in the pixel tracker as shown in Fig. 3.5 to the average measured dE/dx in the strip tracker, shown in Fig. 3.6 by

$$c_{\text{absolute}} = \frac{\langle dE/dx_{\text{strip}} \rangle}{\langle dE/dx_{\text{pixel}} \rangle} = \frac{3.303}{3.509} = 0.941. \quad (3.9)$$

This factor is then applied on top of c_{inter} for all pixel modules.

Finally, an absolute calibration factor needs to be determined for the simulated samples, where the simulated pixel tracker is calibrated to the average dE/dx of the silicon strip measured in data.

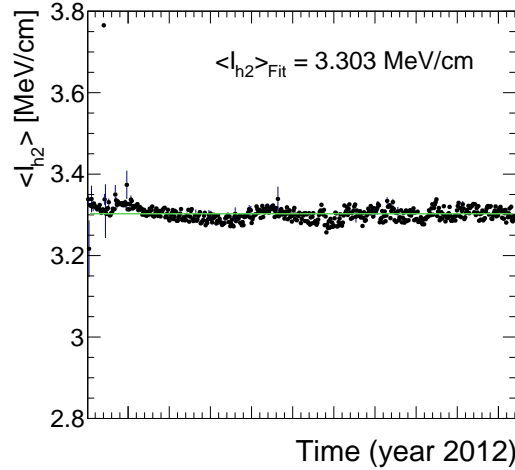


Figure 3.6: Mean of all track's dE/dx (harmonic-2 estimator) measured in the silicon strip detector over the full year 2012. The average most probable dE/dx is $I_{h2} = 3.303$ MeV/cm. Every data point corresponds to one run.

3.3 Discrimination of highly-ionising particles

As mentioned before, it is difficult to find a robust estimator for the most probable energy loss of a particle, if only a few measurements of $\Delta E/\Delta x$ along the particle's trajectory are available. The harmonic-2 estimator I_{h2} was already introduced in Section 3.1 in Eq. (3.4). It is known to be a robust estimator not easily affected by large fluctuations in $\Delta E/\Delta x$. However, it was shown in [23] that a better discrimination between SM particles and possible new heavy particles can be achieved when using likelihood techniques, i. e. determining the probability that the set of all $\Delta E/\Delta x$ belonging to one track is actually compatible with the hypothetical probability distribution of a MIP.

That a measured sample has been drawn from a specific distribution can be tested with the co-called Smirnov-Cramér-von Mises test [25, 26]. It is deduced from the integral of the squared difference of a measured distribution to a hypothesis distribution, and leads to a test statistics of [23]

$$I_s = \frac{3}{N} \cdot \left(\frac{1}{12N} + \sum_{i=1}^N \left[P_i - \frac{2i-1}{2N} \right]^2 \right), \quad (3.10)$$

where N is the total number of energy measurements and P_i is the cumulative probability that a MIP would release a $\Delta E/\Delta x$ equal or smaller than the measured $\Delta E/\Delta x$ with all P_i arranged in increasing order.

However, this test statistics is not sensitive to the sign of the difference between the measured and the theoretical distribution. It can therefore not distinguish between incompatibilities due to variations towards higher or lower energy deposits compared to the hypothesis distribution. Thus it is not suitable for the discrimination between MIPs and heavy new particles by dE/dx . A so-called Asymmetric Smirnov-Cramér-von Mises discriminator was developed in [23] which is only sensitive to incompatibilities to the MIP hypothesis towards higher energy depositions

$$I_{as} = \frac{3}{N} \cdot \left(\frac{1}{12N} + \sum_{i=1}^N \left[P_i \cdot \left(P_i - \frac{2i-1}{2N} \right)^2 \right] \right). \quad (3.11)$$

A value of I_{as} close to zero indicates good compatibility with the MIP hypothesis, whereas a value close to one indicates bad compatibility because of unexpectedly high energy losses.

The underlying probability P_i of the energy release for a given path length in the pixel tracker is extracted from the same “minimum bias” sample used for the pixel energy calibration. In total 28 different templates each for a different given path length are created. In Fig. 3.7 the probability distribution template for the pixel tracker in data and simulation is shown. The corresponding templates for the energy release in the silicon strip detector were already built by [23].

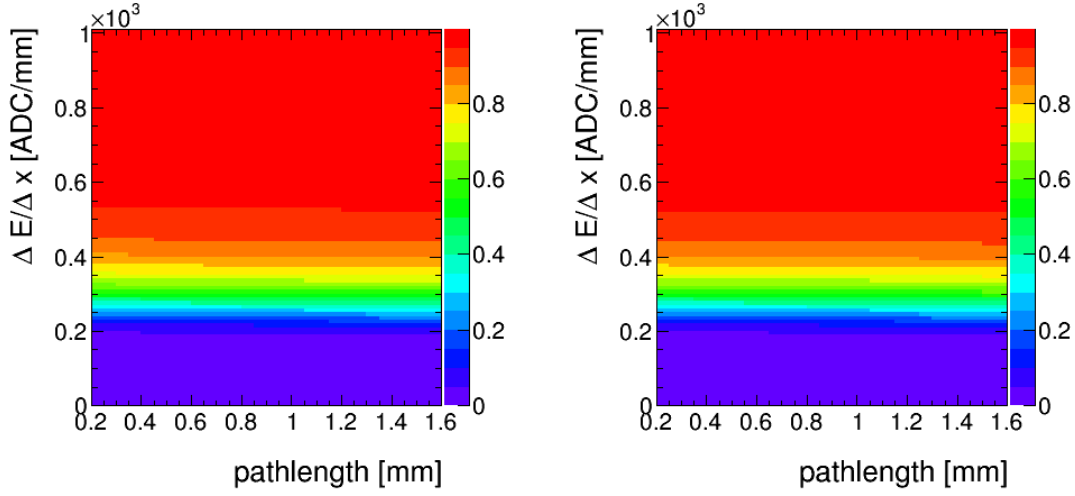


Figure 3.7: Cumulative probability for a MIP to release a $\Delta E/\Delta x$ (y-axis) vs. the pathlength (x-axis) in data (left) and simulation (right) for the pixel tracker based on the “minimum bias” sample.

A comparison between the energy release by MIPs (I_{as}) in data and simulation for high-quality tracks with $p > 5 \text{ GeV}$ and $|\eta| < 2.1$ can be found in Fig. 3.8.

dE/dx shows good agreement in data and simulation for $I_{\text{as}} < 0.1$. For larger values, I_{as} shows a larger decrease in simulation than in measured data. For this reason a data-based approach for analyses exploiting dE/dx information is needed.

3.4 Discrimination improvements

The goal of including the pixel energy information is to increase the discrimination power of I_{as} between background and signal tracks, especially for shorter lifetimes. In Fig. 3.9, a comparison of the shapes of the energy release by MIPs and by signal tracks in simulation is shown (details about the simulated samples can be found in the next section Section 4.2). It can be seen, that the I_{as} distributions of all signal models show a larger tail towards $I_{\text{as}} = 1$, whereas the I_{as} of the background is rapidly falling. The I_{as} distribution is not only influenced by the velocity (β) of a particle but also by the number of hits of a track. The influence of the velocity can be easily seen in Eq. (3.3). This in turn results in a dependency of I_{as} on the mass of the incident particle. However, also for charginos

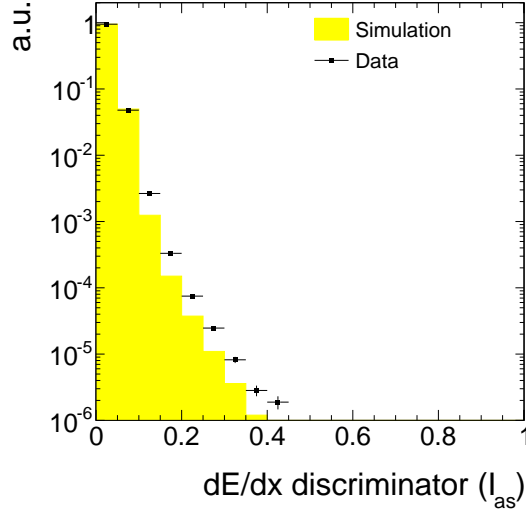


Figure 3.8: Normalised I_{as} distribution for MIPs from the minimum bias sample in data and simulation for high-quality (high purity as defined in [27], a minimum number of eight hits and no missing inner and middle hits) tracks with $p > 5 \text{ GeV}$ and $|\eta| < 2.1$.

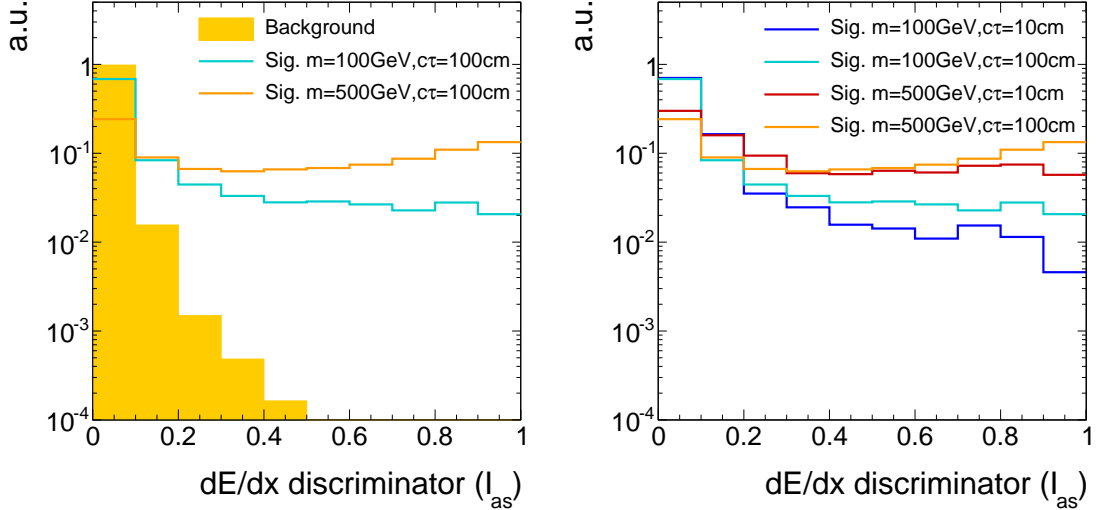


Figure 3.9: Normalised I_{as} distribution for simulated background and signal tracks (left) and for four different signal models (right) for high-purity tracks (as defined in [27]) with $p_{\text{T}} > 10 \text{ GeV}$ and $|\eta| < 2.1$. For the illustration of the background tracks' spectrum simulated $t\bar{t}$ +jets events are used (more information about this sample is given in Section 4).

with same mass, the velocity is higher in average for shorter lifetimes. This is caused by the fact, that for shorter lifetimes (e.g. $c\tau = 10$ cm), already a sizable fraction of the charginos decay before reaching the tracker system. The probability of reaching the detector increases for higher velocities because of the boost, which can be clearly seen at the survival probability

$$P(t) = e^{-\frac{t}{\gamma\tau}}. \quad (3.12)$$

This means that the track reconstruction/selection lead to a biased average β for shorter lifetimes which in turn lead to lower values of I_{as} .

The number of measurements in the tracker system defines the influence of single fluctuations in $\Delta E/\Delta x$ on the I_{as} discriminator, because of the long right tail of the Landau distribution, A low number of hits lead therefore to higher I_{as} values.

Thus, I_{as} for charginos with lower lifetimes are affected by two things: First, due to the smaller number of measurements the chargino tends to higher I_{as} values. Second, low lifetimes charginos have in average a higher velocity leading to lower I_{as} values. Both effects can be seen in Fig. 3.9 (right). The large tail for longer lifetimes is caused by the lower velocities, but the small surplus between 0.1 and 0.2 is caused by the smaller number of measurements for lower lifetimes.

Finally, the impact of the additional $\Delta E/\Delta x$ information from the pixel tracker on the selection efficiency of signal and background tracks is quantified. Figure 3.10 shows the signal selection efficiency against the background selection efficiency for different selection cuts in I_{as} , once including the pixel information and once without it. The background selection efficiency is estimated with simulated W +jets events but was additionally checked on simulated $t\bar{t}$ +jets and QCD-multijet events (further information about the simulated samples can be found in the next section). No significant difference between these processes in the background selection efficiency was observed.

The signal selection efficiency and the background suppression depend on the mass and the lifetime of the charginos. The discrimination power of I_{as} is much better for higher masses as expected.

It can be seen that the inclusion of the pixel information increases the background suppression for a given signal efficiency throughout the investigated signal models. This background suppression improvement is most pronounced for very tight cuts on I_{as} (up to a factor of 20) and still considerable for looser selections with signal efficiencies of around 40% (factor of 10).

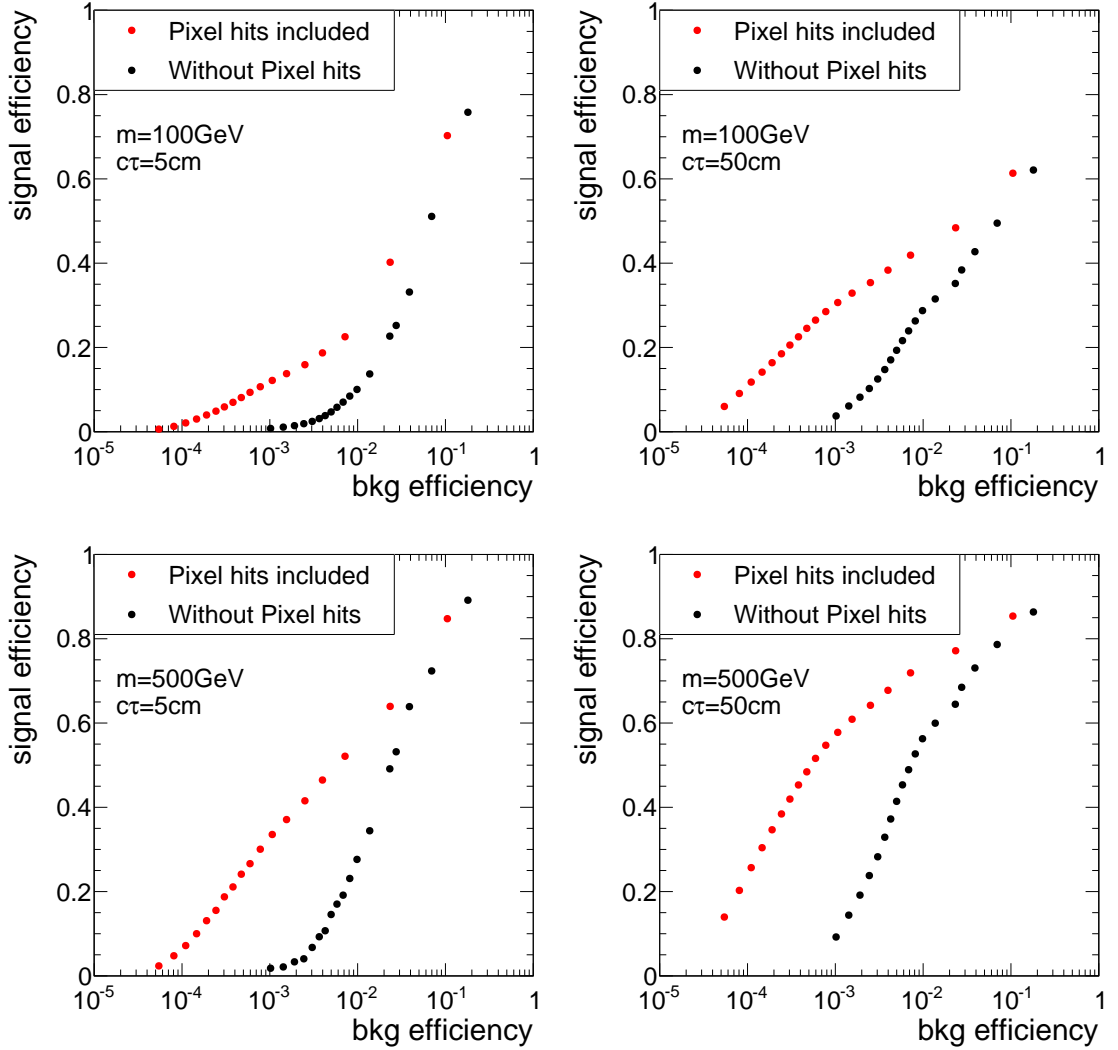


Figure 3.10: Signal selection efficiency vs. background selection efficiency with (red) and without (black) pixel information. Each point correspond to one selection cut in I_{as} . The figure is based on a simulated $W + \text{jets}$ sample and a simulated signal sample with chargino-chargino production, both subject to a selection of high-quality tracks (without a selection on N_{hits}) with $p_T > 10 \text{ GeV}$.

4 Simulated samples

In order to design the search and to study background and signal characteristics, this analysis relies on simulated SM and SUSY datasets. An extensive introduction to the techniques and tools required for the simulation of SM and beyond SM processes can be found in Section ??.

The following two sections present an overview of the SM (Section 4.1) and SUSY samples (Section 4.2) used in this search. All samples are reweighted to match the measured distribution of primary vertices per event in data. Additionally, event weights are applied to ensure the same ISR spectrum in simulation as in data.

4.1 Standard Model background samples

To investigate the sources of background, various simulated SM samples are used. Since this analysis aims at making use of dE/dx , a special data format of the simulated samples, the so-called RECO format, is required. Unfortunately, not all SM processes are available in this specific format making it impossible to compare the total number of events in simulation and real data. This, however, does not constitute a serious problem since this analysis will finally use data-based background estimation methods. The simulated SM datasets can still be used to compare the shapes of important distributions in simulation and data.¹ Still, the most important SM background sample including $W + \text{jets}$ events is available. Due to the intrinsic missing energy in $W + \text{jets}$ events and the additional lepton that can fail reconstruction (see Section ?? for further details on the backgrounds) it constitutes the major background to the presented search.

In Table 4.1 all available SM samples used in this analysis are listed. The matrix-elements of the $W + \text{jets}$, $t\bar{t} + \text{jets}$ and $Z \rightarrow \ell\bar{\ell} + \text{jets}$ samples are generated using MADGRAPH 5 [28]. For the QCD sample PYTHIA6 [29] is used for generation. All samples are then passed to PYTHIA 6 to simulate the hadronisation and the showering. The interactions between the particles and the detector material is simulated using GEANT4 [30,31].

Due to the size of the samples (between 5 and 70 TB per sample) a reduction is required in order to limit the storage space requirements. This is achieved by selecting only events

¹For example, the simulated $Z \rightarrow \nu\bar{\nu} + \text{jets}$ sample that can contribute to the background of this search via fake tracks is not available in RECO format. However, as the shape of important observables of fake tracks is independent of the underlying process, this background can be studied with a simulated $W + \text{jets}$ sample.

Table 4.1: Available Standard Model background samples containing $\Delta E/\Delta x$ information that are used for background estimation studies.

Process	Generator	Cross section [pb]	$\mathcal{O}^{\text{cross section calculation}}$
$W + \text{jets}$	MADGRAPH 5	36703.2	NNLO [32]
$t\bar{t} + \text{jets}$	MADGRAPH 5	245.8	NNLO [33]
$Z \rightarrow \ell\bar{\ell} + \text{jets}$ ($\ell = e, \mu, \tau$)	MADGRAPH 5	3531.9	NNLO [32]
QCD ($50 \text{ GeV} < \hat{p}_T < 1400 \text{ GeV}$)	PYTHIA 6	9374794.2	LO

which contain at least one jet with a minimum transverse momentum of $p_T > 60 \text{ GeV}$.

In addition, further simulated samples not containing the energy information are used (so-called AOD samples). Because of their much smaller size, these samples are available in full size. They are needed to study the background inclusively in the variable dE/dx .

4.2 Signal samples

For the investigation of a possible SUSY signal, events containing either chargino pair production $q\bar{q} \rightarrow \tilde{\chi}_1^\pm \tilde{\chi}_1^\mp$ or chargino neutralino production $q\bar{q} \rightarrow \tilde{\chi}_1^\pm \tilde{\chi}_1^0$ are simulated within this thesis. The simulation of the samples is done as described in Section 4.1 for the $W + \text{jets}$ sample. However, a special treatment for long-lived particles is required for this analysis. In order to get a correct detector simulation of the energy loss of long-lived particles that decay after the beam pipe, the decay of the chargino cannot be simulated within MADGRAPH or PYTHIA but needs to be simulated within GEANT4. The decay mode of the chargino is also specified within GEANT4 to a neutralino plus pion decay, $\tilde{\chi}_1^\pm \rightarrow \tilde{\chi}_1^0 \pi^\pm$.

To reduce the required computing sources, the simulation is only done for a few lifetimes (1 cm, 5 cm, 10 cm, 50 cm, 100 cm, 1 000 cm and 10 000 cm). The lifetime is hereby not controlled by changing the mass gap between the chargino and the neutralino but is independently specified within GEANT4. In order to scan in a high resolution over the lifetime space, other lifetimes are generated using lifetime reweighting. The weight for each event depends on the individual proper lifetime of the chargino and is given by

$$w = \prod_{i=1}^n \frac{\tau^{\text{gen}}}{\tau^{\text{target}}} \cdot \exp \left[t_i \cdot \left(\frac{1}{\tau^{\text{gen}}} - \frac{1}{\tau^{\text{target}}} \right) \right],$$

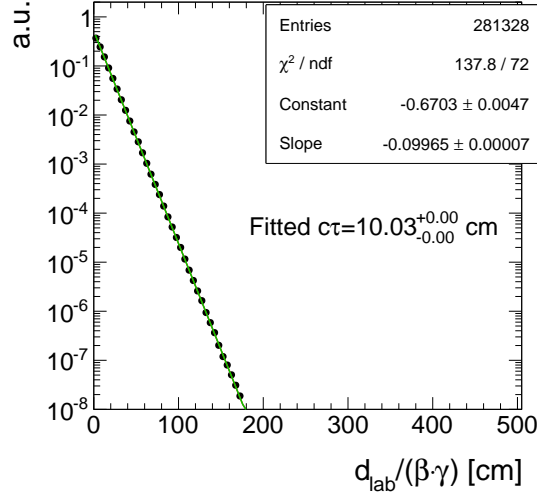


Figure 4.1: Normalised distribution of the proper individual lifetime $d_{\text{lab}}/(\beta\gamma)$ of all charginos contained in a signal sample with a generated lifetime of $c\tau^{\text{gen}} = 50$ cm reweighted to a lifetime of $c\tau^{\text{target}} = 10$ cm. Fitting an exponential curve $a \cdot \exp\left[\frac{1}{c\tau}ct_i\right]$ yields $c\tau = 1./\text{Slope} = 10$ cm.

where n is the number of charginos in the event, τ^{gen} is the generated mean lifetime in the particle's rest frame and t_i is the individual proper lifetime of the chargino. The targeted mean lifetime is given by τ^{target} . A derivation of this formula can be found in Appendix A.1. Using this reweighting procedure a good coverage of the lifetime space can be achieved with lifetimes of $1 \text{ cm} \leq c\tau \leq 10^4 \text{ cm}$. Figure 4.1 shows the exponential distribution of the individual proper lifetime of the charginos after the reweighting of a simulated sample with $c\tau^{\text{gen}} = 50$ cm to a lifetime of $c\tau^{\text{target}} = 10$ cm. It can be seen that the reweighting procedure does indeed reproduce the targeted lifetime of 10 cm.

All samples are generated for different masses of the chargino, but always almost mass-degenerate to the lightest neutralino. The mass gap between chargino and neutralino is set to 150 MeV and, as said before, is hereby disentangled to the chargino lifetime for the simulation of the signal samples. However, since this analysis does not make use of the decay products of the chargino and the mass gap is for all simulated lifetimes of a similar small size, the choice of the mass gap does not affect the signal prediction. Six different masses from 100 GeV to 600 GeV are simulated. This leads to a total number of 42 signal samples. In Table 4.2 cross sections at $\sqrt{s} = 8$ TeV for $\tilde{\chi}_1^\pm \tilde{\chi}_1^\mp$ and $\tilde{\chi}_1^\pm \tilde{\chi}_1^0$ production for wino-like charginos and neutralinos are listed [34, 35]. The cross section does not depend on the lifetime of the chargino.

Table 4.2: Simulated signal mass points with corresponding cross sections at NLO-NLL (NLO: next-to-leading order, NLL: next-to-leading logarithmic) accuracy for wino-like charginos.

$m_{\tilde{\chi}_1^\pm}$ [GeV]	$\sigma_{\tilde{\chi}_1^\pm \tilde{\chi}_1^\mp}$ [pb]	$\sigma_{\tilde{\chi}_1^0 \tilde{\chi}_1^\mp}$ [pb]
100	5.8234	11.5132
200	0.37924	0.77661
300	0.06751	0.14176
400	0.01751	0.03758
500	0.00553	0.01205
600	0.00196	0.00431

5 Event selection

5.1 Datasets and triggers

The analysis is performed on pp collision data recorded in the year 2012 by the CMS experiment at a centre-of-mass energy of $\sqrt{s} = 8$ TeV. In total an integrated luminosity of 19.7 fb^{-1} was recorded in 2012.

As outlined in Section 2, the detection of chargino tracks is a challenging task already on trigger level. Direct triggering of events containing chargino-like tracks is not possible because in 2012 there was no dedicated track trigger available. Furthermore, there is no intrinsic missing transverse energy in the event if the chargino is not reconstructed as a PF particle, e. g. when it decays inside the tracker. Therefore, this analysis uses initial state radiation for the detection of chargino events. If ISR occurs, it is possible to trigger on a high- p_T jet ($p_T^{\text{1st jet}}$) and missing transverse energy (\cancel{E}_T).

For this purpose, several triggers are utilised in this analysis. An event is selected, if at least one of the three triggers in Table 5.1 fired.

The HLTMonoCentralPFJet80_PFMETnoMu95_NHEF0p95 and HLTMonoCentralPFJet80_PFMETnoMu105_NHEF0p95 triggers both rely on the L1 ETM40 trigger which

Table 5.1: \cancel{E}_T and \cancel{E}_T + jet triggers used in this analysis together with the corresponding recorded integrated luminosity during the time when they were in place.

Trigger	Luminosity [fb^{-1}]
HLTMonoCentralPFJet80_PFMETnoMu95_NHEF0p95	5.3
HLTMonoCentralPFJet80_PFMETnoMu105_NHEF0p95	14.4
HLT_MET120_HBHENoiseCleaned	19.7

requires the missing energy to be larger than 40 GeV. On HLT level, they further require at least one particle-flow jet within the pseudorapidity range of $|\eta| < 2.6$ with $p_T > 80$ GeV and a missing transverse momentum (not taking into account the p_T of muons) to be larger than 95 GeV or 105 GeV respectively. Finally, no more than 95% of the jet energy must be carried by neutral hadrons. The HLTMonoCentralPFJet80_PFMETnoMu95_NHEF0p95 trigger was active during Run A and Run B in 2012 data taking, whereas HLTMonoCentralPFJet80_PFMETnoMu105_NHEF0p95 was in place during Run C and Run D in 2012.

The HLT_MET120_HBHENoiseCleaned trigger is based on the L1 trigger ETM36. On HLT level, the trigger requires that the missing energy measured in the calorimeter is larger than 120 GeV. The HBHENoise-filter reduces background from electronic noise in the HCAL.

The events that were selected by the described triggers are available in the MET datasets listed in Table 5.2. Again, because of the size of the datasets (~ 150 TB in total), a re-

Table 5.2: MET data samples used in the search with the contained integrated luminosity.

Dataset	Luminosity [fb^{-1}]
/MET/Run2012A-22Jan2013-v1/RECO	0.876
/MET/Run2012B-22Jan2013-v1/RECO	4.412
/MET/Run2012C-22Jan2013-v1/RECO	7.055
/METParked/Run2012D-22Jan2013-v1/RECO	7.354

duction of the size is achieved by selecting only events where one of the used triggers fired and that contain at least one jet with a minimum p_T of 50 GeV.

5.2 Selection of signal candidate events

In order to suppress events originating from Standard Model processes such as QCD-multijet events, $W + \text{jets}$, etc., a selection favouring signal-like tracks is applied. The signal candidate selection closely follows the selection required in the disappearing track search [36, 37]. It relies on event-based and track-based variables as described in the following two sections.

5.2.1 Event-based selection

First a selection on the quality of the primary vertex is applied in order to suppress cosmic events and noise from the beam halo. This selection includes requirements on the position of the vertex with respect to the beam axes and the number of degrees of freedom of the vertex [38]

- ❖ The vertex must have at least four degrees of freedom: vtx with ≥ 4 d.o.f.
- ❖ The position of the vertex along the beam line must be within 24 cm with respect to the nominal interaction point: $|dz| \leq 24$ cm.
- ❖ The position in the transverse direction must be within 2 cm with respect to the nominal interaction point: $|d0| \leq 2$ cm.

To maximise the signal acceptance, the trigger related selection cuts are chosen close to the trigger thresholds (see Section 5.1). In Fig. 5.1, the distributions of \cancel{E}_T and the transverse momentum of the leading jet, $p_T^{1st\text{ jet}}$, are shown for different signal models. The leading jet has to be centrally produced, $|\eta_{1st\text{ jet}}| < 2.4$, and to fulfil the following criteria:

- Charged hadron energy fraction ($CHF_{1st\text{ jet}}$) > 0.2
- Charged electromagnetic energy fraction ($CEF_{1st\text{ jet}}$) < 0.5
- Neutral hadron energy fraction ($NHF_{1st\text{ jet}}$) < 0.7
- Neutral electromagnetic energy fraction ($NEF_{1st\text{ jet}}$) < 0.7 .

These additional jet quality criteria ensure that noise from cosmic and beam halo muons and high- p_T photons and electrons is suppressed [39].

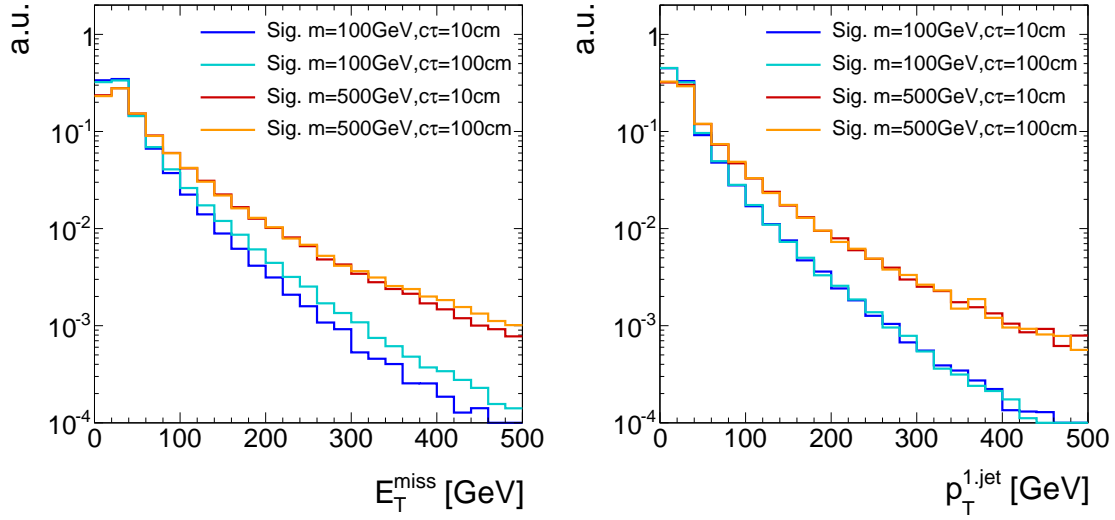


Figure 5.1: Normalised distributions of the missing transverse momentum (left) and the transverse momentum of the leading jet (right) for four different signal models.

The trigger efficiency as a function of \cancel{E}_T and $p_T^{1st\,jet}$ was determined within [40] with a single-muon reference sample. The trigger paths become fully efficient for $p_T^{1st\,jet} \gtrsim 110$ GeV and $\cancel{E}_T \gtrsim 220$ GeV [39]. However, it can be seen in Fig. 5.1 that for a selection of $\cancel{E}_T > 220$ GeV more than 99% of the signal events are rejected.

In order to achieve a reasonable signal acceptance, this search imposes, therefore, a trigger selection closer to the intrinsic trigger thresholds. The trigger requirements are as follows:

- ❖ There is at least one jet within $|\eta| < 2.4$ with transverse momentum larger than 110 GeV which fulfils the above mentioned jet noise cleaning criteria: $p_T^{1st\,jet} > 110$ GeV.
- ❖ The missing transverse momentum must be larger than 100 GeV: $\cancel{E}_T > 100$ GeV

These requirements result in a trigger efficiency of 100% related to the trigger jet p_T requirement and $\sim 5 - 20\%$ in the trigger \cancel{E}_T requirement at the cut thresholds [39]. Throughout the following sections, these trigger related requirements will be referred to as “trigger selection”.

Because of the huge cross section, QCD-multijet events are frequently produced at the LHC. Due to jet energy mismeasurements, they can also contribute to data samples recorded with MET triggers. Therefore, special requirements are enforced in order to suppress events emerging from QCD-multijet processes. QCD-multijet events can be characterised by topologies where two jets are almost back-to-back. Additionally, in QCD-multijet events the missing energy is usually aligned with one of the leading jets in the

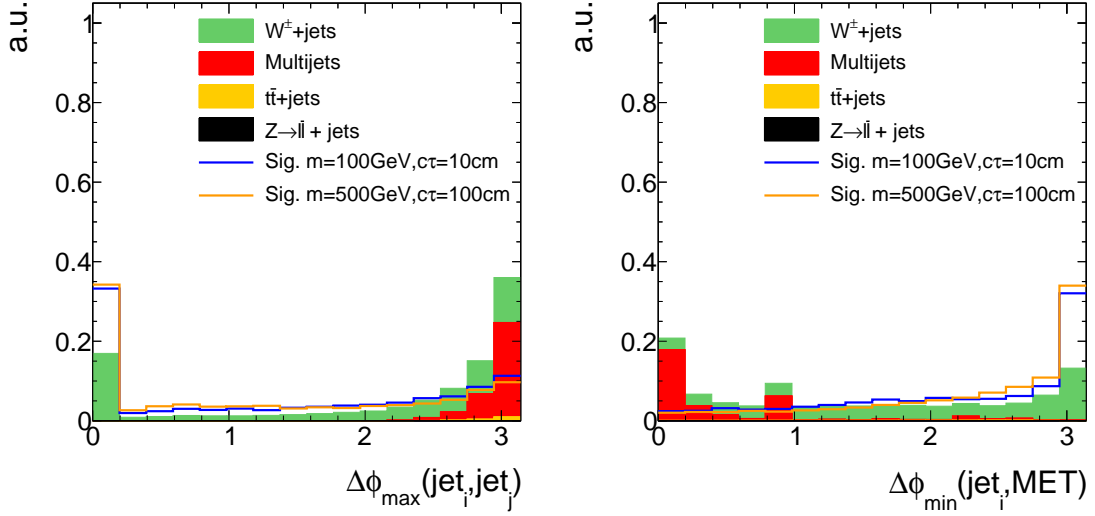


Figure 5.2: Maximum $\Delta\phi$ between any of two jets (left) and the minimum $\Delta\phi$ between the \cancel{E}_T vector and any of the two leading jets (right) normalised to unit area after trigger selection. Only jets with $p_T > 20$ GeV and $|\eta| < 4.5$ are considered.

event. Figure 5.2 shows the maximum $\Delta\phi$ of any of two jets and the minimum $\Delta\phi$ between the \cancel{E}_T vector and any of the two leading jets for the SM background and two different signal datasets.

The following two requirements are sufficient to suppress QCD-multijet events efficiently:

- ❖ $\Delta\phi$ between any of two jets (with $p_T > 20$ GeV and $|\eta| < 4.5$) in the event must be smaller than 2.5.
- ❖ $\Delta\phi$ between any of the two leading jets (with $p_T > 20$ GeV and $|\eta| < 4.5$) and the \cancel{E}_T must be larger than 0.5.

5.2.2 Candidate track selection

After the reduction of background processes with event-based variables, a track-based selection is carried out. To get an optimised selection for possible chargino tracks several signal candidate track characteristics are exploited.

First, a selection of high-quality tracks is enforced:

- ❖ The track must be classified as “high purity” as defined in [27].
- ❖ The track is required to have no missing middle or inner hits: $N_{\text{miss}}^{\text{middle/inner}} = 0$

- ❖ The radial and longitudinal distance of the track to the primary vertex must be small: $|d0| < 0.02 \text{ cm}$, $|dz| < 0.5 \text{ cm}$.

In Figs. 5.3 and 5.4, the power of the latter two quality selection cuts is shown.

Furthermore, a first kinematic preselection is applied:

- ❖ Only tracks in the central region are considered : $|\eta| < 2.1$.
- ❖ Only tracks with a minimum transverse momentum of 20 GeV are considered:
 $p_T > 20 \text{ GeV}$.

In order to suppress background tracks emerging from SM processes, an electron, muon and tau veto is applied. This rejects tracks that are close to a reconstructed electron, muon or tau. Additionally, the candidate track must not be close to a jet ($p_T > 20 \text{ GeV}$ and $|\eta| < 4.5$):

- ❖ The track must not be within a cone of $\Delta R < 0.15$ to a reconstructed standalone, tracker or global muon with a transverse momentum larger than 10 GeV (see Section ?? for details on the different muon definitions).
- ❖ The track must not be within a cone of $\Delta R < 0.15$ to a reconstructed electron with a transverse momentum larger than 10 GeV (see Section ?? for details on the electron reconstruction).

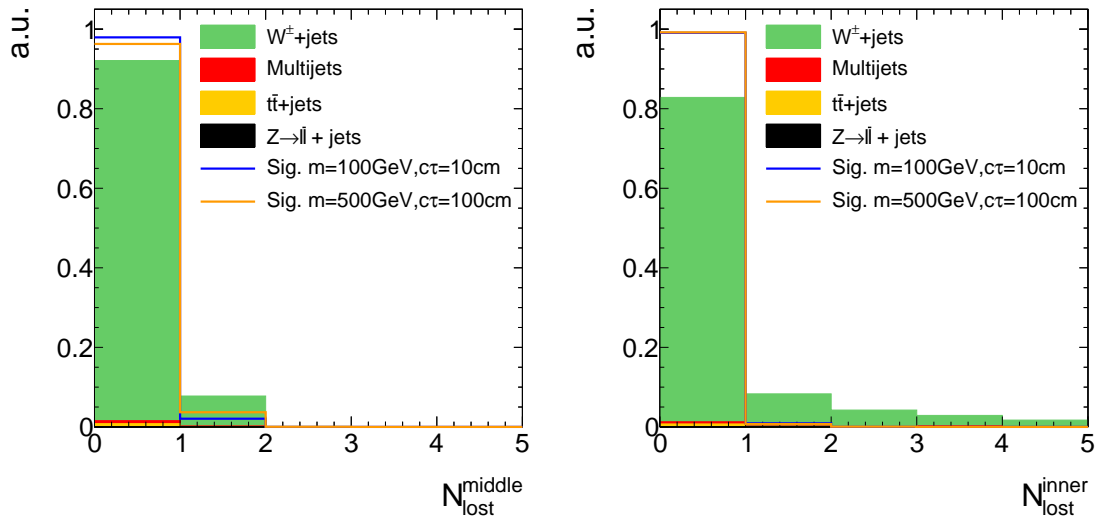


Figure 5.3: Normalised number of missing middle (left) and inner (right) hits of background and signal tracks after trigger selection and QCD suppression cuts.

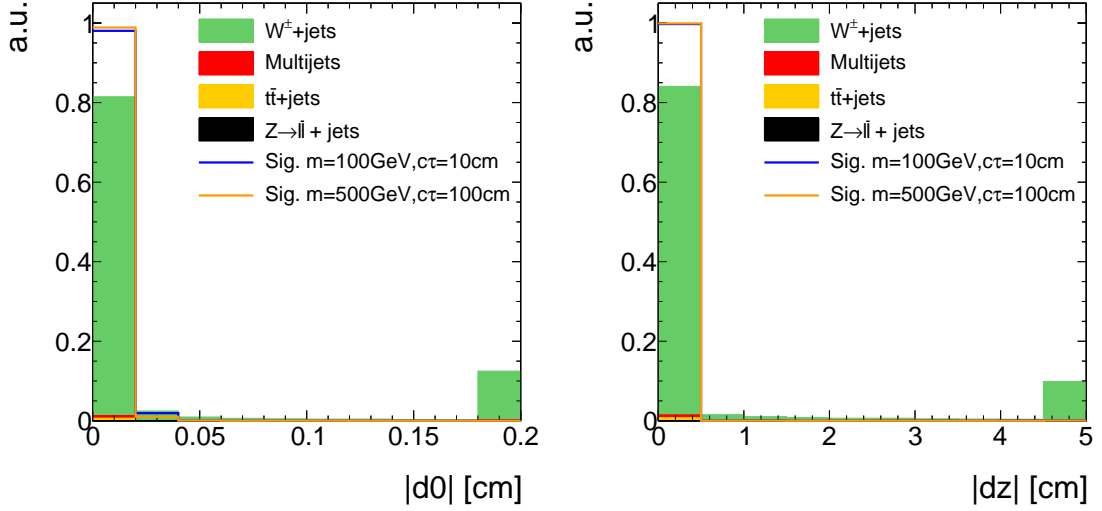


Figure 5.4: Absolute value of the radial (left) and longitudinal (right) distance between the track and the primary vertex after trigger selection and QCD-multijet suppression cuts. All events with a candidate track with a radial (longitudinal) distance larger than 0.2 cm (5 cm) are contained in the last bin.

- ❖ The track must not be within a cone of $\Delta R < 0.15$ to a reconstructed tau with $p_T > 20$ GeV and $|\eta| < 2.3$ (see Section ?? for details on the tau reconstruction). Some loose isolation requirements are enforced to protect the tau reconstruction from jet contamination.
- ❖ The track must not be within a cone of $\Delta R < 0.5$ to a reconstructed jet ($p_T > 20$ GeV and $|\eta| < 4.5$).

Unfortunately, the lepton veto selection cuts lack efficiency in some of the detector directions. For example, the reconstruction of an electron easily fails in the direction of a dead ECAL cell. This reduces the discrimination power of the electron veto. For this reason, tracks that point towards dead or noisy ECAL cells are rejected. A general list of dead and noisy ECAL cells is provided centrally at CMS. Further dead cells were identified within a study in [36,37] resulting in a total number of 1234 dead or noisy ECAL channels. These are illustrated in Fig. 5.5 showing a map of all ECAL channels not considered in the search.

Additionally, tracks that point towards intermodule gaps of ECAL cells or to the ECAL barrel endcap gap at $1.42 < |\eta| < 1.65$ are rejected. A list of the ECAL intermodule gaps, that is supplied centrally at CMS, is given in Table 5.3.

The muon reconstruction is less efficient for muons in detector regions with bad cathode

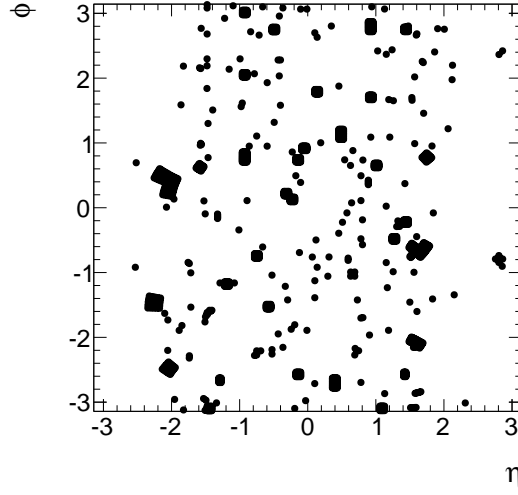


Figure 5.5: Visualisation of dead and noisy ECAL cells in the detector's $\phi - \eta$ plane according to [36, 37]. The radius of the dots correspond to $\Delta R = 0.05$.

strip chambers (CSC). These bad chambers are also identified centrally at CMS and their η and ϕ values are visualised in Fig. 5.6. Thus, also tracks pointing towards these regions within a distance of $\Delta R < 0.25$ are rejected.

To summarise, tracks pointing towards detector regions, that are not working properly or where the lepton reconstruction efficiencies are reduced, are vetoed as follows:

- ❖ Veto tracks within a cone of $\Delta R < 0.05$ to a dead or noisy ECAL cell (visualised in

Table 5.3: Intermodule ECAL gaps.

η -ranges
$-1.14018 < \eta < -1.1439$
$-0.791884 < \eta < -0.796051$
$-0.44356 < \eta < -0.447911$
$0.00238527 < \eta < -0.00330793$
$0.446183 < \eta < 0.441949$
$0.793955 < \eta < 0.789963$
$1.14164 < \eta < 1.13812$

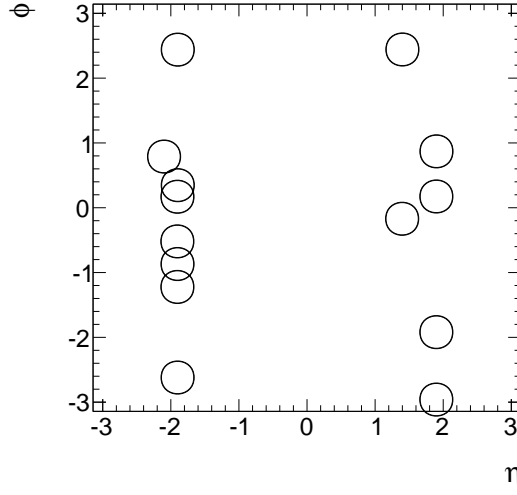


Figure 5.6: Visualisation of the excluded region by the bad cathode strip chamber veto in the detector's $\phi - \eta$.

Fig. 5.5).

- ❖ Veto tracks that point towards the direction of the ECAL intermodule gap listed in Table 5.3.
- ❖ Veto tracks that point towards a bad CSC within $\Delta R < 0.25$ (visualised in Fig. 5.6).
- ❖ Veto tracks that point towards the region between ECAL barrel and endcap at $1.42 < |\eta| < 1.65$

These lepton and jet veto selection requirements are of course highly suppressing the background emerging from real lepton/jet production like in $W + \text{jets}$ events. The discrimination power of the lepton and jet vetos is shown in Fig. 5.7 where the minimum ΔR between the candidate track and a reconstructed electron, muon, tau or jet is shown.

Finally, two further characteristics of chargino tracks are exploited. As the chargino is produced in a very clean environment (no further track activity around the chargino is expected), the isolation of the track can discriminate signal against background events.

Furthermore, for charginos decaying inside the tracker there is no associated energy deposition in the calorimeters in the direction of the track. This is a very pronounced characteristics of signal tracks.

The resulting selection cuts are as follows

- ❖ No further substantial track activity is allowed in a cone of $\Delta R < 0.3$ around the candidate track: $\sum_{\Delta R < 0.3} p_T^{\text{trk}}/p_T^{\text{cand}} - 1 < 0.1$

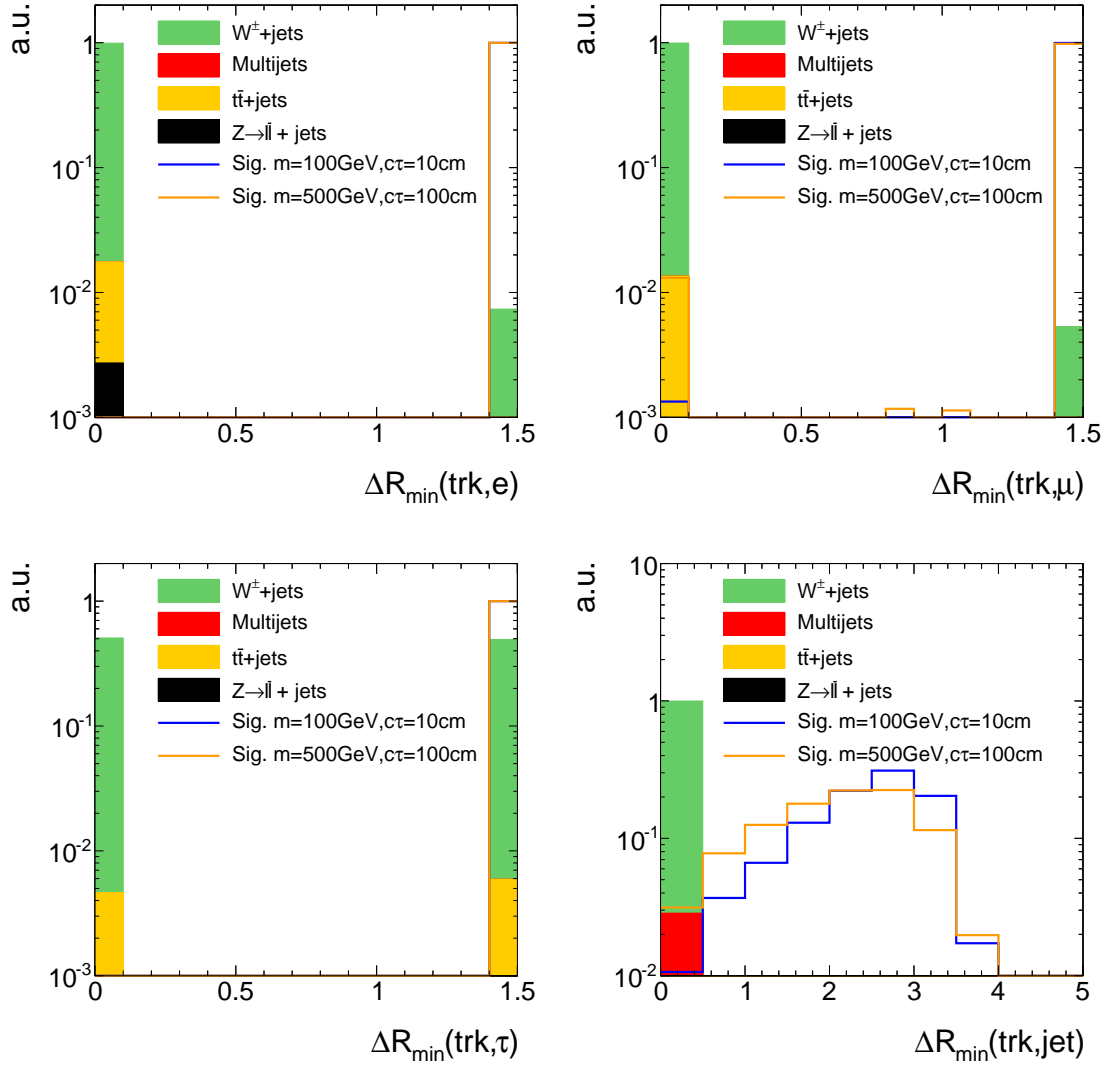


Figure 5.7: The minimum ΔR between the candidate track and a reconstructed electron (top left), muon (top right), tau (bottom left) or jet (bottom right) after the full candidate track selection cuts but without the one shown in the corresponding plot (“N-1 plot”). The last bin contains all events where the candidate track has a ΔR_{\min} larger than 1.5 or 5.0 to the next lepton or jet respectively. Events with no respective lepton or jet are all contained in the last bin.

686 ♦ Little calorimeter energy deposits (ECAL+HCAL) in a cone of $\Delta R < 0.5$ around
 687 the track: $E_{\text{calo}}^{\Delta R < 0.5} < 5 \text{ GeV}$.

688 The discrimination power of these two variables is shown in Fig. 5.8.

689

690 As emphasised before, this analysis aims at being sensitive especially on shorter lifetimes.

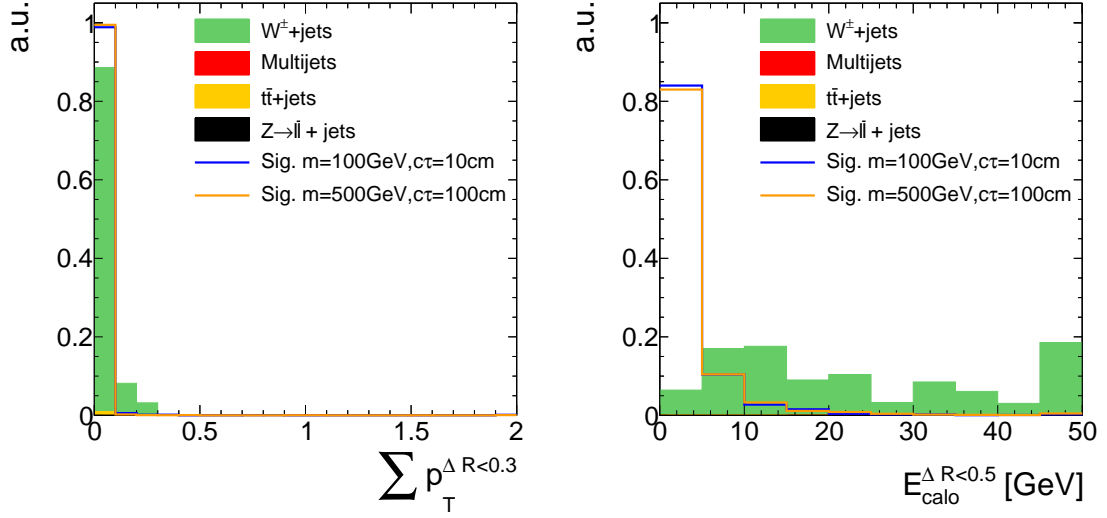


Figure 5.8: Track isolation (left) and calorimeter energy deposits (right) of the candidate track after the full previous selection. All events with a track isolation or a calorimeter energy deposit larger than the range shown in the figures are contained in the last bin.

Still, in order to allow for charginos decaying at any layer of the tracker, no explicit selection cut on the number of missing outer hits is required.

Events are selected if they at least contain one track fulfilling all candidate track selection requirements. An overview over the full analysis preselection is given in Table 5.4. A summary table of the event yields after each selection step for the simulated background datasets and for some of the signal models can be found in Appendix A.2.

Given the presented signal candidate selection, two variables remain that are highly discriminating: The transverse momentum p_T and the energy release per path length dE/dx of the candidate track. In this analysis, the Asymmetric Smirnov discriminator I_{as} is used to enhance the discriminating power of dE/dx . See Section 3.3 for the definition and a detailed explanation of I_{as} .

In Fig. 5.9, the distribution of the remaining two variables are shown after the selection of signal candidate events. These variables are used to optimise the sensitivity of the search. The optimisation process will be explained in Section ???. However, before the optimisation can be accomplished, a characterisation and estimation of the background is needed. This topic will be discussed in the following section.

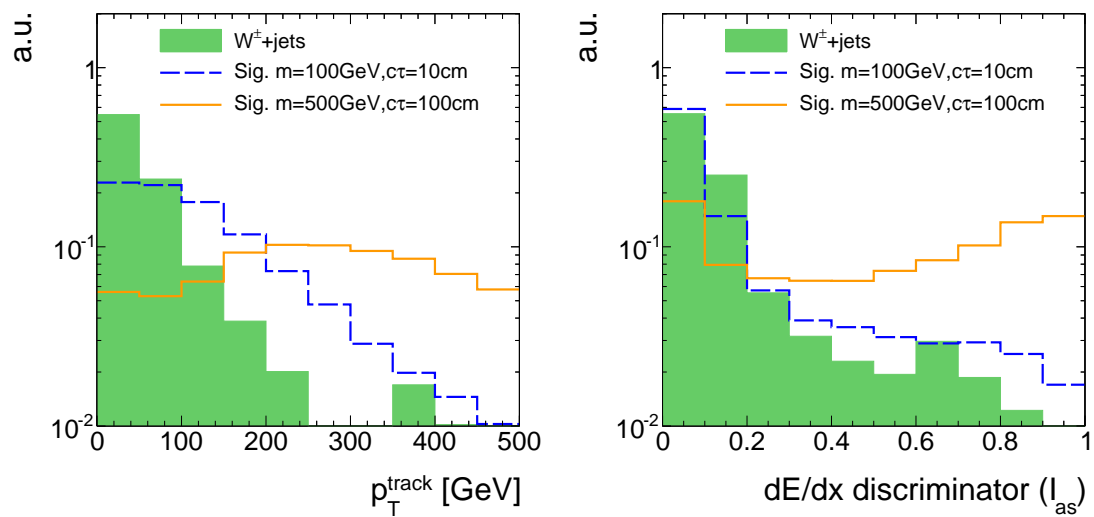


Figure 5.9: Candidate track p_T (left) and I_{as} (right) after the full signal candidate selection for signal and $W + \text{jets}$ events. Because of the low statistical precision of the $W + \text{jets}$ sample, the trigger selection is not applied.

Table 5.4: Summary and categorisation of the analysis selection.

Trigger	HLTMonoCentralPFJet80_PFMETnoMu95_NHEF0p95	
	HLTMonoCentralPFJet80_PFMETnoMu105_NHEF0p95	
	HLT_MET120_HBHENoiseCleaned	
Event-based selection	Trigger selection	$p_T^{1^{\text{st}} \text{jet}} > 100 \text{ GeV}$ with $ \eta_{1^{\text{st}} \text{jet}} < 2.4$, $\text{CHF}_{1^{\text{st}} \text{jet}} > 0.2$, $\text{CEF}_{1^{\text{st}} \text{jet}} < 0.5$, $\text{NHF}_{1^{\text{st}} \text{jet}} < 0.7$, $\text{NEF}_{1^{\text{st}} \text{jet}} < 0.7$ $\cancel{E}_T > 100 \text{ GeV}$
	QCD suppression	$\Delta\phi_{\text{max}}(\text{jet}_i, \text{jet}_j) < 2.7$ for all jets with $p_T > 20 \text{ GeV}$, $ \eta < 4.5$ $\Delta\phi_{\text{max}}(\text{jet}_i, \cancel{E}_T) > 0.5$ for two leading jets
Candidate track selection	≥ 1 track that fulfils the following criteria:	
	Good quality selection	high-purity as defined in [27] $N_{\text{miss}}^{\text{middle/inner}} = 0$ $ d0 < 0.02 \text{ cm}$ $ dz < 0.5 \text{ cm}$
	Kinematic selection	$ \eta < 2.1$ $p_T > 10 \text{ GeV}$
	Lepton/jet veto	No muon within $\Delta R < 0.15$ No electron within $\Delta R < 0.15$ No tau within $\Delta R < 0.15$ No jet within $\Delta R < 0.5$ No dead/noisy ECAL cell within $\Delta R < 0.05$ Not within an ECAL intermodule gap Not within $1.42 < \eta < 1.65$ Not within $\Delta R < 0.25$ to a bad CSC
	Isolation selection	$\sum_{\Delta R < 0.3} p_T^{\text{trk}} / p_T^{\text{cand}} - 1 < 0.1$ $E_{\text{calo}}^{\Delta R < 0.5} < 5 \text{ GeV}$

A A search for highly ionising, short tracks

A.1 Lifetime reweighting

The probability density function of a particle's proper lifetime for a sample generated with a particle's mean lifetime τ^{gen} is given by

$$p(t) = \frac{1}{\tau^{\text{gen}}} \cdot \exp\left[-\frac{t}{\tau^{\text{gen}}}\right].$$

After carrying out the lifetime reweighting procedure, the targeted p.d.f of the particle's new mean lifetime τ^{target} is given by

$$p'(t) = \frac{1}{\tau^{\text{target}}} \cdot \exp\left[-\frac{t}{\tau^{\text{target}}}\right].$$

Thus, an event containing a particle with individual proper lifetime can be reweighted with the following weight

$$w = \frac{p'(t)}{p(t)} = \frac{\tau^{\text{gen}}}{\tau^{\text{target}}} \cdot \exp\left[\frac{t}{\tau^{\text{gen}}} - \frac{t}{\tau^{\text{target}}}\right].$$

For more than one non-stable particle, the event weight is calculated by multiplying the weights of the single reweighting procedures.

A.2 Event yields for simulated samples and data

Table A.1: Event yields after each selection step for various background processes.

Selection	$W + \text{jets}$	$t\bar{t} + \text{jets}$	$Z \rightarrow \ell\bar{\ell}$	Multijet
after skim	$9.16 \cdot 10^7$	$1.04 \cdot 10^6$	$2.21 \cdot 10^7$	$1.38 \cdot 10^{11}$
trigger	$4.31 \cdot 10^6$	$1.15 \cdot 10^5$	$4.23 \cdot 10^3$	$4.32 \cdot 10^6$
$p_T^{\text{1st jet}} > 110 \text{ GeV}$	$2.47 \cdot 10^6$	$7.17 \cdot 10^4$	$2.60 \cdot 10^3$	$2.75 \cdot 10^6$
$\cancel{E}_T > 100 \text{ GeV}$	$1.89 \cdot 10^6$	$5.31 \cdot 10^4$	$6.26 \cdot 10^2$	$9.63 \cdot 10^5$
$\Delta\phi_{\text{max}}(\text{jet}_i, \text{jet}_j) < 2.7$	$1.11 \cdot 10^6$	$6.81 \cdot 10^3$	$1.32 \cdot 10^2$	$2.01 \cdot 10^4$
$\Delta\phi_{\text{max}}(\text{jet}_{1,2}, \cancel{E}_T) > 0.5$	$1.11 \cdot 10^6$	$6.76 \cdot 10^3$	$1.32 \cdot 10^2$	$9.55 \cdot 10^3$
≥ 1 track in the event with:				
reconstructed trk	$1.10 \cdot 10^6$	$6.75 \cdot 10^3$	$1.32 \cdot 10^2$	$9.55 \cdot 10^3$
high-purity	$1.10 \cdot 10^6$	$6.74 \cdot 10^3$	$1.32 \cdot 10^2$	$9.55 \cdot 10^3$
$N_{\text{miss}}^{\text{middle}} = 0$	$1.09 \cdot 10^6$	$6.72 \cdot 10^3$	$1.32 \cdot 10^2$	$9.55 \cdot 10^3$
$N_{\text{miss}}^{\text{inner}} = 0$	$1.07 \cdot 10^6$	$6.70 \cdot 10^3$	$1.32 \cdot 10^2$	$9.55 \cdot 10^3$
$ d0 < 0.02 \text{ cm}$	$1.07 \cdot 10^6$	$6.64 \cdot 10^3$	$1.32 \cdot 10^2$	$9.55 \cdot 10^3$
$ dz < 0.5 \text{ cm}$	$1.07 \cdot 10^6$	$6.63 \cdot 10^3$	$1.32 \cdot 10^2$	$9.55 \cdot 10^3$
$ \eta < 2.1$	$1.03 \cdot 10^6$	$6.58 \cdot 10^3$	$1.32 \cdot 10^2$	$9.55 \cdot 10^3$
$p_T > 20 \text{ GeV}$	$8.14 \cdot 10^5$	$5.63 \cdot 10^3$	$1.32 \cdot 10^2$	$5.48 \cdot 10^3$
No μ within $\Delta R < 0.15$	$7.15 \cdot 10^5$	$4.52 \cdot 10^3$	$1.32 \cdot 10^2$	$5.48 \cdot 10^3$
No e within $\Delta R < 0.15$	$6.69 \cdot 10^5$	$3.67 \cdot 10^3$	$7.86 \cdot 10^1$	$5.48 \cdot 10^3$
No τ within $\Delta R < 0.15$	$6.62 \cdot 10^5$	$3.61 \cdot 10^3$	$7.86 \cdot 10^1$	$5.47 \cdot 10^3$
No jet within $\Delta R < 0.5$	$1.18 \cdot 10^3$	$1.44 \cdot 10^1$	$1.09 \cdot 10^1$	$0.00 \cdot 10^0$
Not within $\Delta R < 0.05$ of a dead/noisy ECAL cell	$7.25 \cdot 10^2$	$8.02 \cdot 10^0$	$0.00 \cdot 10^0$	$0.00 \cdot 10^0$
Not within an ECAL intermodule gap	$7.15 \cdot 10^2$	$8.02 \cdot 10^0$	$0.00 \cdot 10^0$	$0.00 \cdot 10^0$
Not within $1.42 < \eta < 1.65$	$5.89 \cdot 10^2$	$6.53 \cdot 10^0$	$0.00 \cdot 10^0$	$0.00 \cdot 10^0$
Not within $\Delta R < 0.25$ to a bad CSC	$5.02 \cdot 10^2$	$5.88 \cdot 10^0$	$0.00 \cdot 10^0$	$0.00 \cdot 10^0$
$\sum_{\Delta R < 0.3} p_T^{\text{trk}}/p_T^{\text{cand}} - 1 < 0.1$	$4.46 \cdot 10^2$	$4.78 \cdot 10^0$	$0.00 \cdot 10^0$	$0.00 \cdot 10^0$
$E_{\text{calo}}^{\Delta R < 0.5} < 5 \text{ GeV}$	$3.19 \cdot 10^1$	$0.67 \cdot 10^0$	$0.00 \cdot 10^0$	$0.00 \cdot 10^0$

Table A.2: Event yields after each selection step for various signal models.

Selection	m=100 GeV $c\tau=10$ cm	m=100 GeV $c\tau=100$ cm	m=500 GeV $c\tau=10$ cm	m=500 GeV $c\tau=100$ cm
total	$3.41 \cdot 10^5$	$3.41 \cdot 10^5$	$3.46 \cdot 10^2$	$3.46 \cdot 10^2$
trigger	$1.55 \cdot 10^4$	$1.49 \cdot 10^4$	$4.62 \cdot 10^1$	$4.62 \cdot 10^1$
$p_T^{\text{1st jet}} > 110$ GeV	$1.10 \cdot 10^4$	$1.04 \cdot 10^4$	$3.64 \cdot 10^1$	$3.58 \cdot 10^1$
$\cancel{E}_T > 100$ GeV	$1.09 \cdot 10^4$	$9.83 \cdot 10^3$	$3.63 \cdot 10^1$	$3.57 \cdot 10^1$
$\Delta\phi_{\text{max}}(\text{jet}_i, \text{jet}_j) < 2.7$	$7.90 \cdot 10^3$	$7.04 \cdot 10^3$	$2.76 \cdot 10^1$	$2.72 \cdot 10^1$
$\Delta\phi_{\text{max}}(\text{jet}_{1,2}, \cancel{E}_T) > 0.5$	$7.90 \cdot 10^3$	$6.98 \cdot 10^3$	$2.76 \cdot 10^1$	$2.71 \cdot 10^1$
≥ 1 track in the event with:				
reconstructed trk	$3.13 \cdot 10^3$	$5.74 \cdot 10^3$	$5.74 \cdot 10^0$	$2.13 \cdot 10^1$
high-purity	$2.91 \cdot 10^3$	$5.65 \cdot 10^3$	$5.25 \cdot 10^0$	$2.08 \cdot 10^1$
$N_{\text{miss}}^{\text{middle}} = 0$	$2.87 \cdot 10^3$	$5.46 \cdot 10^3$	$5.23 \cdot 10^0$	$2.02 \cdot 10^1$
$N_{\text{miss}}^{\text{inner}} = 0$	$2.86 \cdot 10^3$	$5.40 \cdot 10^3$	$5.22 \cdot 10^0$	$2.01 \cdot 10^1$
$ d0 < 0.02$ cm	$2.81 \cdot 10^3$	$5.39 \cdot 10^3$	$5.07 \cdot 10^0$	$2.00 \cdot 10^1$
$ dz < 0.5$ cm	$2.80 \cdot 10^3$	$5.38 \cdot 10^3$	$5.07 \cdot 10^0$	$2.00 \cdot 10^1$
$ \eta < 2.1$	$2.63 \cdot 10^3$	$4.97 \cdot 10^3$	$5.01 \cdot 10^0$	$1.91 \cdot 10^1$
$p_T > 20$ GeV	$2.54 \cdot 10^3$	$4.93 \cdot 10^3$	$4.73 \cdot 10^0$	$1.89 \cdot 10^1$
No μ within $\Delta R < 0.15$	$2.54 \cdot 10^3$	$4.65 \cdot 10^3$	$4.72 \cdot 10^0$	$1.87 \cdot 10^1$
No e within $\Delta R < 0.15$	$2.54 \cdot 10^3$	$4.65 \cdot 10^3$	$4.72 \cdot 10^0$	$1.87 \cdot 10^1$
No τ within $\Delta R < 0.15$	$2.54 \cdot 10^3$	$4.64 \cdot 10^3$	$4.72 \cdot 10^0$	$1.87 \cdot 10^1$
No jet within $\Delta R < 0.5$	$2.53 \cdot 10^3$	$4.59 \cdot 10^3$	$4.63 \cdot 10^0$	$1.82 \cdot 10^1$
Not within $\Delta R < 0.05$ of a dead/noisy ECAL cell	$2.32 \cdot 10^3$	$4.25 \cdot 10^3$	$4.19 \cdot 10^0$	$1.69 \cdot 10^1$
Not within an ECAL intermodule gap	$2.31 \cdot 10^3$	$4.23 \cdot 10^3$	$4.17 \cdot 10^0$	$1.68 \cdot 10^1$
Not within $1.42 < \eta < 1.65$	$2.09 \cdot 10^3$	$3.88 \cdot 10^3$	$3.95 \cdot 10^0$	$1.56 \cdot 10^1$
Not within $\Delta R < 0.25$ to a bad CSC	$1.99 \cdot 10^3$	$3.67 \cdot 10^3$	$3.83 \cdot 10^0$	$1.50 \cdot 10^1$
$\sum_{\Delta R < 0.3} p_T^{\text{trk}}/p_T^{\text{cand}} - 1 < 0.1$	$1.97 \cdot 10^3$	$3.64 \cdot 10^3$	$3.78 \cdot 10^0$	$1.49 \cdot 10^1$
$E_{\text{calo}}^{\Delta R < 0.5} < 5$ GeV	$1.67 \cdot 10^3$	$3.04 \cdot 10^3$	$3.39 \cdot 10^0$	$1.26 \cdot 10^1$

Table A.3: Observed event yield after each selection step in data.

Selection	MET dataset
after skim	$1.07 \cdot 10^7$
trigger	$1.07 \cdot 10^7$
$p_{\text{T}}^{\text{1st jet}} > 110 \text{ GeV}$	$6.82 \cdot 10^6$
$\cancel{E}_{\text{T}} > 100 \text{ GeV}$	$3.94 \cdot 10^6$
$\Delta\phi_{\text{max}}(\text{jet}_i, \text{jet}_j) < 2.7$	$1.39 \cdot 10^6$
$\Delta\phi_{\text{max}}(\text{jet}_{1,2}, \cancel{E}_{\text{T}}) > 0.5$	$1.38 \cdot 10^6$
≥ 1 track in the event with:	
reconstructed trk	$1.37 \cdot 10^6$
high-purity	$1.36 \cdot 10^6$
$N_{\text{miss}}^{\text{middle}} = 0$	$1.34 \cdot 10^6$
$N_{\text{miss}}^{\text{inner}} = 0$	$1.31 \cdot 10^6$
$ d0 < 0.02 \text{ cm}$	$1.30 \cdot 10^6$
$ dz < 0.5 \text{ cm}$	$1.30 \cdot 10^6$
$ \eta < 2.1$	$1.26 \cdot 10^6$
$p_{\text{T}} > 20 \text{ GeV}$	$9.51 \cdot 10^5$
No μ within $\Delta R < 0.15$	$8.40 \cdot 10^5$
No e within $\Delta R < 0.15$	$8.01 \cdot 10^5$
No τ within $\Delta R < 0.15$	$7.95 \cdot 10^5$
No jet within $\Delta R < 0.5$	$1.75 \cdot 10^3$
Not within $\Delta R < 0.05$ of a dead/noisy ECAL cell	$9.11 \cdot 10^2$
Not within an ECAL intermodule gap	$9.06 \cdot 10^2$
Not within $1.42 < \eta < 1.65$	$7.33 \cdot 10^2$
Not within $\Delta R < 0.25$ to a bad CSC	$6.16 \cdot 10^2$
$\sum_{\Delta R < 0.3} p_{\text{T}}^{\text{trk}}/p_{\text{T}}^{\text{cand}} - 1 < 0.1$	$5.26 \cdot 10^2$
$E_{\text{calo}}^{\Delta R < 0.5} < 5 \text{ GeV}$	$1.19 \cdot 10^2$
$p_{\text{T}} > 30 \text{ GeV}$	$9.10 \cdot 10^1$
$I_{\text{as}} > 0.05$	$5.60 \cdot 10^1$

A.3 Signal contamination in validation regions

Signal contamination in the four validation regions from Section ?? . The highest signal contamination is visible for a lifetime of 100 cm for all signal masses. For higher lifetimes the signal contamination is again reduced due to the muon veto selection requirement. The most extreme values (from $c\tau = 100$ cm) of expected signal events and some other selected signal models are shown in the following tables. The signal contamination is rapidly falling towards lower lifetimes and higher masses.

Table A.4: Signal contamination in leptonic control region: $E_{\text{calo}}^{\Delta R < 0.5} > 10$ GeV and $N_{\text{hits}} > 6$. N_S is the number of expected signal events and ΔB is the statistical uncertainty on the background prediction.

Signal model	N_S	$N_S/\Delta B$	Excluded by [11]
mass=100 GeV, $c\tau = 100$ cm	211.93	8.06	yes
mass=100 GeV, $c\tau = 10$ cm	27.83	1.06	yes
mass=100 GeV, $c\tau = 5$ cm	7.39	0.28	yes
mass=100 GeV, $c\tau = 1$ cm	0	0	no
mass=300 GeV, $c\tau = 100$ cm	6.97	0.26	yes
mass=300 GeV, $c\tau = 10$ cm	0.33	0.01	yes
mass=300 GeV, $c\tau = 5$ cm	0.0	0.0	no
mass=500 GeV, $c\tau = 100$ cm	0.72	0.03	yes
mass=500 GeV, $c\tau = 10$ cm	0.00	0.00	no

Table A.5: Signal contamination in leptonic control region: $E_{\text{calo}}^{\Delta R < 0.5} > 10 \text{ GeV}$, $N_{\text{hits}} > 6$ and $I_{\text{as}} > 0.2$. N_S is the number of expected signal events and ΔB is the statistical uncertainty on the background prediction.

Signal model	N_S	$N_S/\Delta B$	Excluded by [11]
mass=100 GeV, $c\tau = 100 \text{ cm}$	24.11	48.21	yes
mass=100 GeV, $c\tau = 10 \text{ cm}$	0.00	0.00	yes
mass=300 GeV, $c\tau = 100 \text{ cm}$	2.03	4.06	yes
mass=300 GeV, $c\tau = 10 \text{ cm}$	0.03	0.07	yes
mass=300 GeV, $c\tau = 5 \text{ cm}$	0.0	0.0	no
mass=500 GeV, $c\tau = 100 \text{ cm}$	0.38	0.75	yes
mass=500 GeV, $c\tau = 10 \text{ cm}$	0.00	0.00	no

Table A.6: Signal contamination in fake+lepton control region: $E_{\text{calo}}^{\Delta R < 0.5} > 10 \text{ GeV}$. N_S is the number of expected signal events and ΔB is the statistical uncertainty on the background prediction.

Signal model	N_S	$N_S/\Delta B$	Excluded by [11]
mass=100 GeV, $c\tau = 100 \text{ cm}$	257.33	7.69	yes
mass=100 GeV, $c\tau = 10 \text{ cm}$	116.21	3.47	yes
mass=100 GeV, $c\tau = 5 \text{ cm}$	48.07	1.44	yes
mass=100 GeV, $c\tau = 1 \text{ cm}$	1.26	0.04	no
mass=300 GeV, $c\tau = 100 \text{ cm}$	9.35	0.28	yes
mass=300 GeV, $c\tau = 10 \text{ cm}$	2.20	0.07	yes
mass=300 GeV, $c\tau = 5 \text{ cm}$	0.85	0.03	no
mass=500 GeV, $c\tau = 100 \text{ cm}$	1.10	0.03	yes
mass=500 GeV, $c\tau = 10 \text{ cm}$	0.15	0.00	no

Table A.7: Signal contamination in fake+lepton control region: $E_{\text{calo}}^{\Delta R < 0.5} > 10 \text{ GeV}$, and $I_{\text{as}} > 0.2$. N_S is the number of expected signal events and ΔB is the statistical uncertainty on the background prediction.

Signal model	N_S	$N_S/\Delta B$	Excluded by [11]
mass=100 GeV, $c\tau = 100 \text{ cm}$	36.40	12.47	yes
mass=100 GeV, $c\tau = 10 \text{ cm}$	5.22	1.79	yes
mass=100 GeV, $c\tau = 5 \text{ cm}$	1.76	0.60	yes
mass=300 GeV, $c\tau = 100 \text{ cm}$	3.20	1.10	yes
mass=300 GeV, $c\tau = 10 \text{ cm}$	0.58	0.20	yes
mass=300 GeV, $c\tau = 5 \text{ cm}$	0.12	0.04	no
mass=500 GeV, $c\tau = 100 \text{ cm}$	0.63	0.22	yes
mass=500 GeV, $c\tau = 10 \text{ cm}$	0.07	0.02	no

726

A.4 Validation tests of the background estimation methods

Table A.8: Validation tests of the background estimation methods in the calorimeter isolation control region $E_{\text{calo}}^{\Delta R < 0.5} > 10 \text{ GeV}$ for two different p_T selection requirements: $p_T > 40 \text{ GeV}$ (left) and $p_T > 60 \text{ GeV}$ (right). Only statistical uncertainties are included.

	Predicted Yield	Data Yield		Predicted Yield	Data Yield
Total bkg	$84.36^{+16.47}_{-10.88}$	94	Total bkg	$35.56^{+11.95}_{-6.20}$	53
Electrons	$15.69^{+11.92}_{-6.72}$		Electrons	$0.00^{+9.14}_{-0.00}$	
Muons	$5.67^{+7.74}_{-3.55}$		Muons	$3.65^{+4.98}_{-2.28}$	
Taus	$35.78^{+5.09}_{-4.18}$		Taus	$13.22^{+1.88}_{-1.55}$	
Fakes	$27.23^{+6.57}_{-6.57}$		Fakes	$18.70^{+5.55}_{-5.55}$	

Table A.9: Validation tests of the background estimation methods in the calorimeter isolation control region $E_{\text{calo}}^{\Delta R < 0.5} > 10 \text{ GeV}$ with an additional I_{as} selection of $I_{\text{as}} > 0.2$ for two different p_{T} selection requirements: $p_{\text{T}} > 40 \text{ GeV}$ (left) and $p_{\text{T}} > 60 \text{ GeV}$ (right). Only statistical uncertainties are included.

	Predicted Yield	Data Yield		Predicted Yield	Data Yield
Total bkg	$4.76^{+1.42}_{-1.39}$	8	Total bkg	$2.31^{+0.97}_{-0.95}$	3
Electrons	$0.20^{+0.17}_{-0.10}$		Electrons	$0.00^{+0.11}_{-0.00}$	
Muons	$0.00^{+0.22}_{-0.00}$		Muons	$0.00^{+0.14}_{-0.00}$	
Taus	$0.48^{+0.15}_{-0.11}$		Taus	$0.18^{+0.06}_{-0.04}$	
Fakes	$4.08^{+1.38}_{-1.38}$		Fakes	$2.14^{+0.95}_{-0.95}$	

Table A.10: Validation tests of the background estimation methods in the calorimeter isolation control region $E_{\text{calo}}^{\Delta R < 0.5} > 10 \text{ GeV}$ with an additional I_{as} selection of $I_{\text{as}} > 0.4$ for two different p_{T} selection requirements: $p_{\text{T}} > 40 \text{ GeV}$ (left) and $p_{\text{T}} > 60 \text{ GeV}$ (right). Only statistical uncertainties are included.

	Predicted Yield	Data Yield		Predicted Yield	Data Yield
Total bkg	$1.98^{+0.87}_{-0.83}$	2	Total bkg	$1.10^{+0.63}_{-0.61}$	1
Electrons	$0.00^{+0.05}_{-0.00}$		Electrons	$0.00^{+0.00}_{-0.00}$	
Muons	$0.00^{+0.22}_{-0.00}$		Muons	$0.00^{+0.14}_{-0.00}$	
Taus	$0.08^{+0.09}_{-0.04}$		Taus	$0.03^{+0.03}_{-0.02}$	
Fakes	$1.91^{+0.83}_{-0.83}$		Fakes	$1.07^{+0.61}_{-0.61}$	

727 The underprediction in the control regions with $I_{\text{as}} > 0.2$ is caused by the prediction
728 of the leptonic I_{as} shape from simulation. This leads to a bias as the I_{as} distribution in
729 simulation is softer than in data. However, this bias is taken into account as systematic
730 uncertainty (see Section ??).

731

A.5 Selection requirements of the “tag-and-probe” samples

Table A.11: Event selection cuts for the muon “tag-and-probe” samples (T&P signal region sample and T&P lepton veto inverted control region sample) that are used to estimate the uncertainty on the muon scale factor ρ_{MC}^μ .

Muon selection	$p_{\text{T}} > 25 \text{ GeV}$ $ \eta < 2.4$ $\sum_{\Delta R < 0.4} p_{\text{T}}^{\text{PF particle}} / p_{\text{T}}(\mu) < 0.12$ $\frac{\chi^2}{ndof} \Big _{\text{global track}} < 10$ $ d0 < 0.2 \text{ cm}$ $ dz < 0.5 \text{ cm}$ $\geq 1 \text{ hit in the muon detector}$ $\geq 2 \text{ hits in different muon detector planes}$ $\geq 1 \text{ hit in the pixel detector}$ $\geq 6 \text{ hits in the tracker system}$
Candidate track selection	Good quality selection Kinematic selection Lepton/jet veto (μ veto inverted for the “tag-and-probe” control region) Isolation selection $N_{\text{hits}} > 5$
Event-based selection	Muon and candidate track opposite in charge $80 \text{ GeV} < M_{\text{inv}}(\mu, \text{can. trk}) < 100 \text{ GeV}$

Table A.12: Event selection cuts for the tau “tag-and-probe” samples (T&P signal region sample and T&P lepton veto inverted control region sample) that are used to estimate the uncertainty on the tau scale factor ρ_{MC}^τ .

<p>Muon selection that is compatible with a $\tau \rightarrow \mu\nu\nu$ decay</p>	<p>$p_{\text{T}} > 25 \text{ GeV}$ $\eta < 2.4$ $\sum_{\Delta R < 0.4} p_{\text{T}}^{\text{PF particle}} / p_{\text{T}}(\mu) < 0.12$ $\frac{\chi^2}{ndof} \Big _{\text{global track}} < 10$ $d0 < 0.2 \text{ cm}$ $dz < 0.5 \text{ cm}$ ≥ 1 hit in the muon detector ≥ 2 hits in different muon detector planes ≥ 1 hit in the pixel detector ≥ 6 hits in the tracker system</p>
<p>Candidate track selection</p>	<p>Good quality selection Kinematic selection Lepton/jet veto (τ veto inverted for the “tag-and-probe” control region) $\sum_{\Delta R < 0.3} p_{\text{T}}^{\text{trk}} / p_{\text{T}}^{\text{cand}} - 1 < 0.1$ $N_{\text{hits}} > 5$</p>
<p>Event-based selection</p>	<p>Muon and candidate track opposite in charge $40 \text{ GeV} < M_{\text{inv}}(\mu, \text{cand. trk}) < 75 \text{ GeV}$ $m_T(\mu, \cancel{E}_{\text{T}}) < 40 \text{ GeV}$</p>

Table A.13: Event selection cuts for the electron “tag-and-probe” samples (T&P signal region sample and T&P lepton veto inverted control region sample) that are used to estimate the uncertainty on the electron scale factor ρ_{MC}^e .

Electron selection	$p_{\text{T}} > 25 \text{ GeV}$ $ \eta < 2.5$ $\sum_{\Delta R < 0.4} p_{\text{T}}^{\text{PF particle}} / p_{\text{T}}(e) < 0.15$ pass conversion veto no missing tracker hits good MVA electron as defined in [41]
Candidate track selection	Good quality selection Kinematic selection Lepton/jet veto (e veto inverted for the “tag-and-probe” control region) $\sum_{\Delta R < 0.3} p_{\text{T}}^{\text{trk}} / p_{\text{T}}^{\text{cand}} - 1 < 0.1$ $N_{\text{hits}} > 5$
Event-based selection	Electron and candidate track opposite in charge $80 \text{ GeV} < M_{\text{inv}}(e, \text{cand. trk}) < 100 \text{ GeV}$

A.6 Optimisation results with the number of missing outer hits

Also an optimisation in the number of missing outer hits is performed. No significant improvement is visible in the search sensitivity for different selection requirements of $N_{\text{lost}}^{\text{outer}}$, see Fig A.1. This is caused by the fact, that the main background, the fake background,

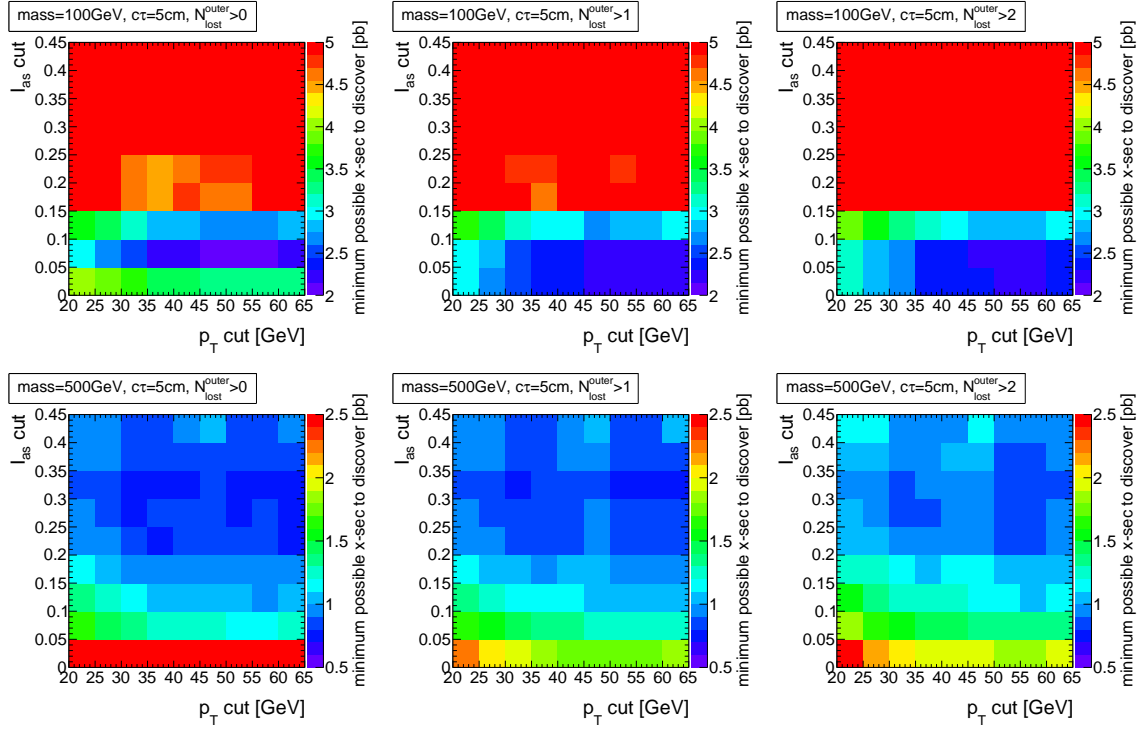


Figure A.1: Minimum possible cross section that can be discovered with 5σ significance in the $I_{\text{as}}p_{\text{T}}$ plane for two different signal models with a chargino lifetime of 5 cm and a mass of 100 GeV (top) and 500 GeV (bottom). The requirement on the number of missing outer hits is varied between $N_{\text{lost}}^{\text{outer}} > 0$ (left), $N_{\text{lost}}^{\text{outer}} > 1$ (middle), $N_{\text{lost}}^{\text{outer}} > 2$ (right). A difference in the sensitivity can be spotted when looking at the lowest value of the minimum cross section that occurs. No sizable discrimination improvement is visible for a tighter selection in $N_{\text{lost}}^{\text{outer}}$.

also shows missing outer hits. A comparison between the number of missing outer hits for the fake background and two signal models is shown in Fig. A.2.

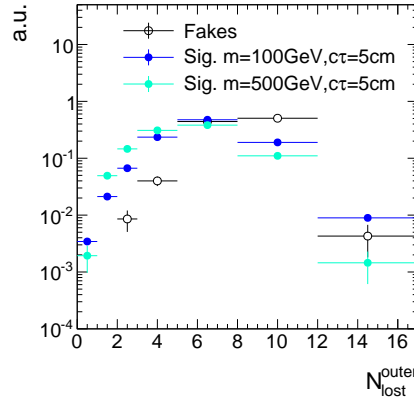


Figure A.2: Normalised distribution of the number of missing outer hits for fake tracks and two different signal models.

A.7 Underlying distributions for the qualitative search sensitivity optimisation

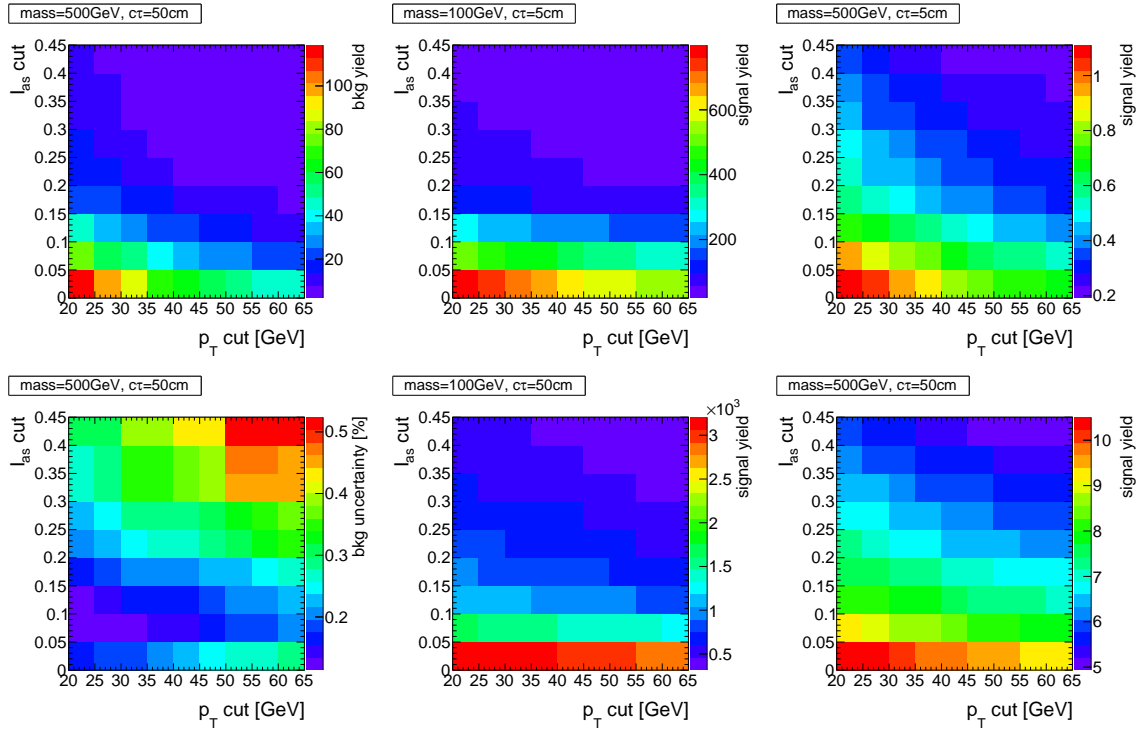


Figure A.3: Background yield, background uncertainty and signal yield for different p_T and I_{as} selection requirements and four different signal models.

740 **A.8 Trigger emulation**

741 As the HLTMonoCentralPFJet80_PFMETnoMu105_NHEF0p95 trigger is not available in
742 the simulated signal samples, this trigger is emulated in these samples. Since HLT trigger
743 information is stored in the samples, it is possible to rebuild the trigger afterwards.

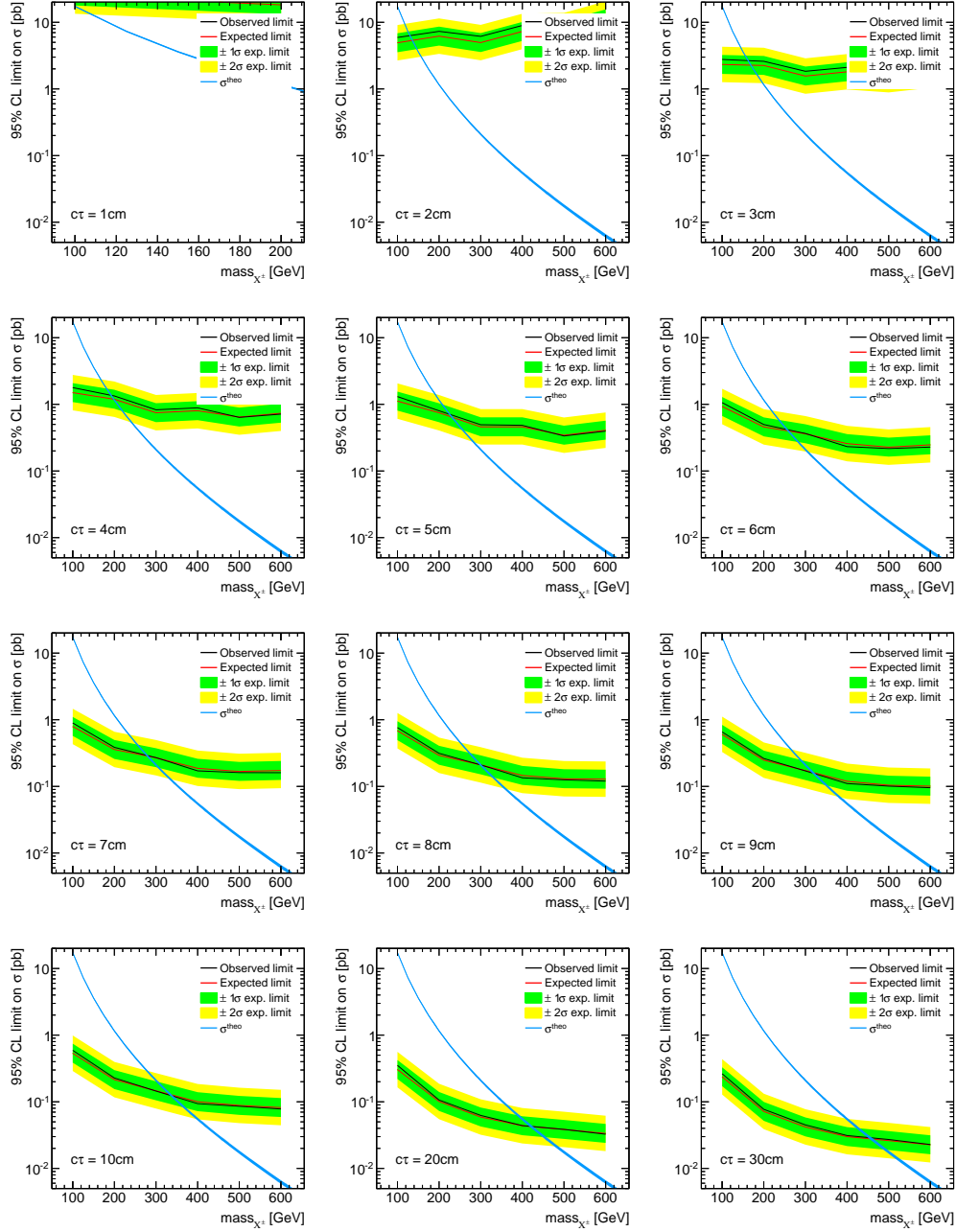
744 The following requirements must be fulfilled in order to consider the trigger firing [36,37]:

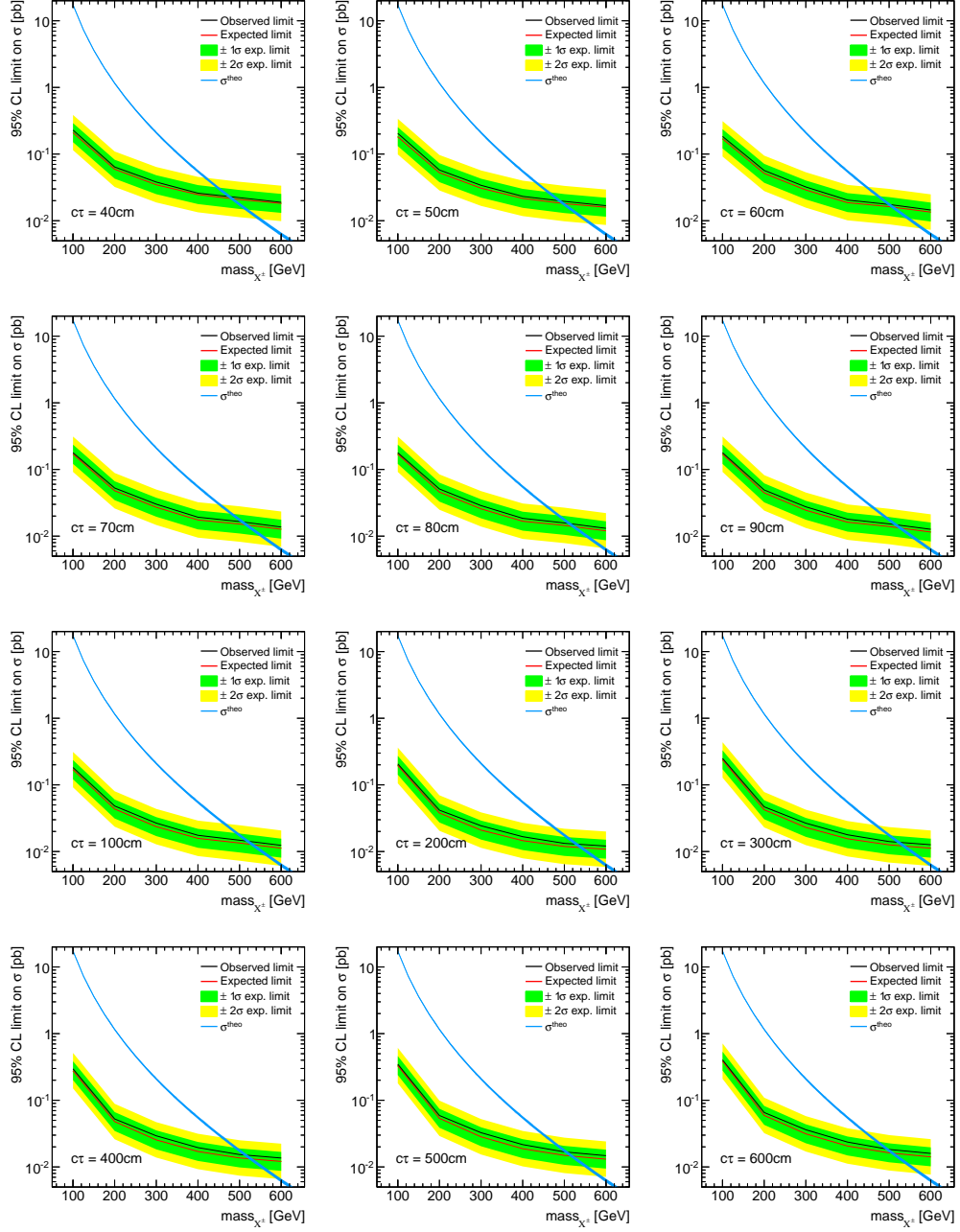
- 745 • p_T of hltL1sL1ETM40 > 40 GeV
- 746 • p_T of hltCentralJet65L1FastJet > 65 GeV
- 747 • p_T of hltMET65 > 65 GeV
- 748 • p_T of hltCentralPFJet80 > 80 GeV
- 749 • p_T of hltPFMETWOM95 > 105 GeV

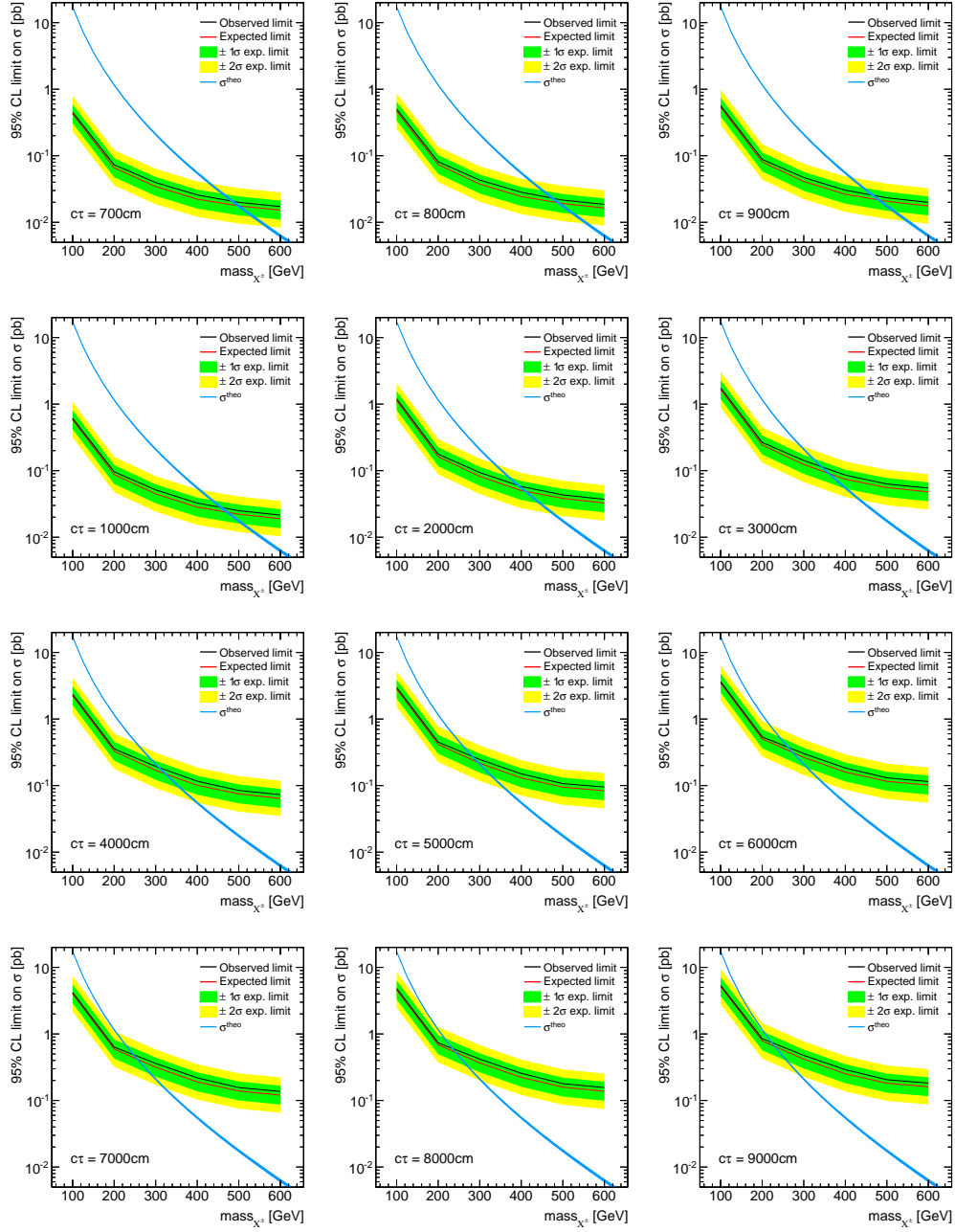
750 As a cross check, also the HLTMonoCentralPFJet80_PFMETnoMu95_NHEF0p95 is re-
751 build with the looser selection of p_T of hltPFMETWOM95 > 95 GeV. The correct imple-
752 mentation could be verified with this test.

753

A.9 Exclusion limits for all simulated lifetimes

Figure A.4: 95% CL exclusion limits for signal models with $c\tau = 1 - 30$ cm.

Figure A.5: 95% CL exclusion limits for signal models with $c\tau = 40 - 600$ cm.

Figure A.6: 95% CL exclusion limits for signal models with $c\tau = 700 - 9000$ cm.

Bibliography

- [1] CDF, D0 Collaboration, T. Adams, “SUSY Searches at the Tevatron”, in *Hadron collider physics. Proceedings, 19th Symposium, HCP2008, Galena, USA, May 27-31, 2008*. 2008. [arXiv:0808.0728](#).
- [2] ALEPH, DELPHI, L3 and OPAL Collaborations, “Joint SUSY Working Group”. <http://http://lepsusy.web.cern.ch/lepsusy/>. LEPSUSYWG (June 2004).
- [3] CMS Collaboration, “Search for new physics in the multijet and missing transverse momentum final state in proton-proton collisions at $\sqrt{s}=8$ TeV”, *JHEP* **06** (2014) 055, [arXiv:1402.4770](#). doi:10.1007/JHEP06(2014)055.
- [4] CMS Collaboration, “Searches for Supersymmetry using the M_{T2} Variable in Hadronic Events Produced in pp Collisions at 8 TeV”, *JHEP* **05** (2015) 078, [arXiv:1502.04358](#). doi:10.1007/JHEP05(2015)078.
- [5] ATLAS Collaboration, “Search for squarks and gluinos with the ATLAS detector in final states with jets and missing transverse momentum using $\sqrt{s}=8$ TeV proton-proton collision data”, *JHEP* **09** (2014) 176, [arXiv:1405.7875](#). doi:10.1007/JHEP09(2014)176.
- [6] T. Moroi and L. Randall, “Wino cold dark matter from anomaly mediated SUSY breaking”, *Nucl. Phys.* **B570** (2000) 455–472, [arXiv:hep-ph/9906527](#). doi:10.1016/S0550-3213(99)00748-8.
- [7] J. Hisano, S. Matsumoto, M. M. Nojiri et al., “Direct detection of the Wino and Higgsino-like neutralino dark matters at one-loop level”, *Phys. Rev.* **D71** (2005) 015007, [arXiv:hep-ph/0407168](#). doi:10.1103/PhysRevD.71.015007.
- [8] M. Ibe, S. Matsumoto, S. Shirai et al., “Wino Dark Matter in light of the AMS-02 2015 Data”, *Phys. Rev.* **D91** (2015), no. 11, 111701, [arXiv:1504.05554](#). doi:10.1103/PhysRevD.91.111701.
- [9] T. Moroi, M. Nagai, and M. Takimoto, “Non-Thermal Production of Wino Dark Matter via the Decay of Long-Lived Particles”, *JHEP* **07** (2013) 066, [arXiv:1303.0948](#). doi:10.1007/JHEP07(2013)066.

- [10] J. Hisano, S. Matsumoto, and M. M. Nojiri, “Explosive dark matter annihilation”, *Phys. Rev. Lett.* **92** (2004) 031303, [arXiv:hep-ph/0307216](#).
[doi:10.1103/PhysRevLett.92.031303](#).
- [11] CMS Collaboration, “Search for disappearing tracks in proton-proton collisions at $\sqrt{s} = 8$ TeV”, *JHEP* **01** (2015) 096, [arXiv:1411.6006](#).
[doi:10.1007/JHEP01\(2015\)096](#).
- [12] CMS Collaboration, “Searches for long-lived charged particles in pp collisions at $\sqrt{s}=7$ and 8 TeV”, *JHEP* **07** (2013) 122, [arXiv:1305.0491](#).
[doi:10.1007/JHEP07\(2013\)122](#).
- [13] CMS Collaboration, “Phenomenological MSSM interpretation of the CMS 2011 5fb-1 results”, *CMS Physics Analysis Summary CMS-PAS-SUS-12-030* (2013).
- [14] CMS Collaboration, “Reinterpreting the results of the search for long-lived charged particles in the pMSSM and other BSM scenarios”, *CMS Physics Analysis Summary CMS-PAS-EXO-13-006* (2014).
- [15] CMS Collaboration, “Search for disappearing tracks in proton-proton collisions at $\sqrt{s} = 8$ TeV”, *Public CMS Wiki* (2015).
<https://twiki.cern.ch/twiki/bin/view/CMSPublic/PhysicsResultsEXO12034>, Topic revision: r9.
- [16] CMS Collaboration, “Search for heavy long-lived charged particles in pp collisions at $\sqrt{s} = 7$ TeV”, *Phys. Lett.* **B713** (2012) 408–433, [arXiv:1205.0272](#).
[doi:10.1016/j.physletb.2012.06.023](#).
- [17] CMS Collaboration, “Description and performance of track and primary-vertex reconstruction with the CMS tracker”, *JINST* **9** (2014), no. 10, P10009,
[arXiv:1405.6569](#). [doi:10.1088/1748-0221/9/10/P10009](#).
- [18] H. Bethe, “Theory of the Passage of Fast Corpuscular Rays Through Matter”, *Annalen Phys.* **5** (1930) 325–400. [Annalen Phys.397,325(1930)].
[doi:10.1002/andp.19303970303](#).
- [19] “National Institute of Standards and Technology”.
<http://physics.nist.gov/cgi-bin/Star/compos.pl?mode=text&matno=014>.
Accessed: 2015-10-21.
- [20] Particle Data Group Collaboration, “Review of Particle Physics”, *Chin. Phys.* **C38** (2014) 090001. [doi:10.1088/1674-1137/38/9/090001](#).

- [21] L. Landau, “On the energy loss of fast particles by ionization”, *J. Phys.(USSR)* **8** (1944) 201–205.
- [22] H. Bichsel, “Straggling in Thin Silicon Detectors”, *Rev. Mod. Phys.* **60** (1988) 663–699. doi:10.1103/RevModPhys.60.663.
- [23] L. Quertenmont, “Search for Heavy Stable Charged Particles with the CMS detector at the LHC”. PhD thesis, Louvain, U., 2010.
<https://inspirehep.net/record/1088192/files/openfile.pdf>.
- [24] D. Kotlinski. personal communication.
- [25] T. W. Anderson, “On the Distribution of the Two-Sample Cramr-von Mises Criterion”, *The Annals of Mathematical Statistics* **33** (1962), no. 3, pp. 1148–1159.
- [26] F. James, “Statistical methods in experimental physics”. 2006.
- [27] CMS Collaboration, “Tracking and Vertexing Results from First Collisions”, *CMS Physics Analysis Summary CMS-PAS-TRK-10-001* (2010).
- [28] J. Alwall, R. Frederix, S. Frixione et al., “The automated computation of tree-level and next-to-leading order differential cross sections, and their matching to parton shower simulations”, *JHEP* **07** (2014) 079, arXiv:1405.0301.
doi:10.1007/JHEP07(2014)079.
- [29] T. Sjostrand, S. Mrenna, and P. Z. Skands, “PYTHIA 6.4 Physics and Manual”, *JHEP* **05** (2006) 026, arXiv:hep-ph/0603175.
doi:10.1088/1126-6708/2006/05/026.
- [30] GEANT4 Collaboration, “GEANT4: A Simulation toolkit”, *Nucl. Instrum. Meth.* **A506** (2003) 250–303. doi:10.1016/S0168-9002(03)01368-8.
- [31] J. Allison et al., “Geant4 developments and applications”, *IEEE Trans. Nucl. Sci.* **53** (2006) 270. doi:10.1109/TNS.2006.869826.
- [32] R. Gavin et al., “FEWZ 3.1: A User’s Guide”.
http://www.hep.anl.gov/fpetriello/FEWZManual_3.1.pdf. Accessed: 2015-10-27.
- [33] M. Czakon, P. Fiedler, and A. Mitov, “Total Top-Quark Pair-Production Cross Section at Hadron Colliders Through $O(\frac{4}{s})$ ”, *Phys. Rev. Lett.* **110** (2013) 252004, arXiv:1303.6254. doi:10.1103/PhysRevLett.110.252004.
- [34] B. Fuks, M. Klasen, D. R. Lamprea et al., “Gaugino production in proton-proton collisions at a center-of-mass energy of 8 TeV”, *JHEP* **1210** (2012) 081, arXiv:1207.2159. doi:10.1007/JHEP10(2012)081.

- [35] B. Fuks, M. Klasen, D. R. Lamprea et al., “Precision predictions for electroweak superpartner production at hadron colliders with Resummino”, *Eur.Phys.J.* **C73** (2013) 2480, [arXiv:1304.0790](#). doi:10.1140/epjc/s10052-013-2480-0.
- [36] J. D. Brinson, “A search for disappearing tracks in proton-proton collisions at $\sqrt{s} = 8$ TeV”. PhD thesis, Ohio State U.
<https://inspirehep.net/record/1381347/files/CERN-THESIS-2015-030.pdf>.
- [37] C. H. J. Brinson and W. Wulsin, “Search for disappearing tracks”, *CMS Analysis Note* **CMS-AN-12-400** (2014). Internal documentation.
- [38] CMS Collaboration, “Tracking and Primary Vertex Results in First 7 TeV Collisions”, *CMS Physics Analysis Summary* **CMS-PAS-TRK-10-005** (2010).
- [39] A. B. et. al., “Search for New Physics in the Monojet final state at CMS”, *CMS Analysis Note* **CMS-AN-12-421** (2012). Internal documentation.
- [40] CMS Collaboration, “Search for dark matter, extra dimensions, and unparticles in monojet events in protonproton collisions at $\sqrt{s} = 8$ TeV”, *Eur. Phys. J.* **C75** (2015), no. 5, 235, [arXiv:1408.3583](#). doi:10.1140/epjc/s10052-015-3451-4.
- [41] CMS Collaboration, “Measurement of Higgs boson production and properties in the WW decay channel with leptonic final states”, *JHEP* **01** (2014) 096, [arXiv:1312.1129](#). doi:10.1007/JHEP01(2014)096.

